A cellular and spatial map of the choroid plexus across brain ventricles and ages

Neil Dani[1,*], **Rebecca H. Herbst**[2,3,*], **Cristin McCabe**[2], **Gilad Green**[4], **Karol Kaiser**[5], **Joshua Head**[1], **Jin Cui**[1], **Frederick B. Shipley**[1,6], **Ahram Jang**[1], **Danielle Dionne**[2], **Lan Nguyen**[2], **Christopher Rodman**[2], **Samantha J. Riesenfeld**[2], **Jan Prochazka**[7], **Michaela Prochazkova**[7], **Radislav Sedlacek**[7], **Feng Zhang**[8,9,10,11], **Vitezslav Bryja**[5], **Orit Rozenblatt-Rosen**[2,13], **Naomi Habib**[8,4,#], **Aviv Regev**[2,8,9,12,13,#], **Maria K. Lehtinen**[1,6,#,†]

[1]Department of Pathology, Boston Children's Hospital, Boston, MA, USA 02115

[2]Klarman Cell Observatory, Broad Institute of MIT and Harvard, Cambridge, MA, USA 02142

[3]Department of Systems Biology, Harvard Medical School, Boston, MA, USA 02115

[4]Edmond and Lily Safra Center for Brain Sciences, Hebrew University of Jerusalem, Jerusalem, Israel 9190401

[5]Department of Experimental Biology, Faculty of Science, Masaryk University, Brno, Czech Republic 611 37

[6]Graduate Program in Biophysics, Harvard University, Cambridge, MA, USA 02115

[7]Czech Centre for Phenogenomics and Laboratory of Transgenic Models of Diseases, Institute of Molecular Genetics of the CAS, Czech Republic 142 20

[8]Broad Institute of MIT and Harvard, Cambridge, MA, USA 02142

[9]Howard Hughes Medical Institute, Chevy Chase, MD, USA 20815

Correspondence should be addressed to: maria.lehtinen@childrens.harvard.edu, naomi.habib@mail.huji.ac.il, aviv.regev.sc@gmail.com.
*Contributed equally.
#Co-senior authors.
†Lead contact: maria.lehtinen@childrens.harvard.edu

AUTHOR CONTRIBUTIONS

DECLARATION OF INTERESTS

[10]McGovern Institute for Brain Research, Massachusetts Institute of Technology, Cambridge, MA, USA 02139

[11]Department of Brain and Cognitive Sciences and Department of Biological Engineering, Massachusetts Institute of Technology, Cambridge, MA, USA 02139

[12]Koch Institute of Integrative Cancer Research, Department of Biology, Massachusetts Institute of Technology, Cambridge, MA, USA 02142

[13]Current address: Genentech, 1 DNA Way, South San Francisco, CA

SUMMARY

The choroid plexus (ChP) in each brain ventricle produces cerebrospinal fluid (CSF) and forms the blood-CSF barrier. Here, we construct a single cell and spatial atlas of each ChP in the developing, adult, and aged mouse brain. We delineate diverse cell types, subtypes, cell states and expression programs in epithelial and mesenchymal cells across ages and ventricles. In the developing ChP, we predict a common progenitor pool for epithelial and neuronal cells, validated by lineage tracing. Epithelial and fibroblast cells showed regionalized expression by ventricle, starting at embryonic stages and persisting with age, with a dramatic transcriptional shift with maturation, and a smaller shift in each aged cell type. With aging, epithelial cells upregulated host defense programs and resident macrophages upregulated IL-1β signaling genes. Our atlas revealed cellular diversity, architecture and signaling across ventricles during development, maturation and aging of the ChP brain barrier.

Graphical Abstract
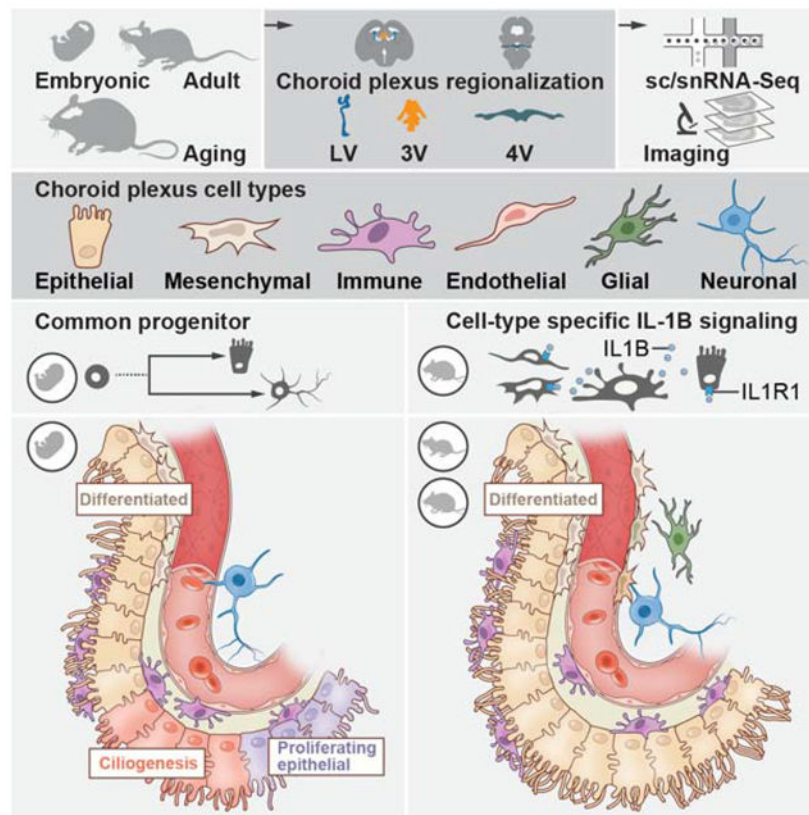
Keywords

Choroid plexus; brain barrier; cerebrospinal fluid; single cell RNA-sequencing; single nucleus RNA-sequencing

INTRODUCTION

The choroid plexus (ChP) is an essential brain barrier known primarily as a source of cerebrospinal fluid (CSF) and comprises an analogous set of four tissue structures located in each brain ventricle. The foundation of the ChP is an epithelial sheet that, together with a network of vasculature and diverse cell types, regulates CSF secretion and governs its composition by *de novo* protein synthesis and selective transcytosis of blood-borne factors (Damkier et al., 2013; Ghersi-Egea et al., 2018; Lun et al., 2015a; Saunders et al., 2018b). In addition, the ChP participates in regulating neurogenesis (Lehtinen et al., 2011; Silva-Vargas et al., 2016), homeostatic responses to arousal states (Mathew et al., 2016; Myung et al., 2018), inflammatory signals (Cui et al., 2020; Van Hove et al., 2019; Jordão et al., 2019a; Karimy et al., 2017; Reboldi et al., 2009; Schwartz and Baruch, 2014; Shechter et al., 2013), and atypical courses of neurodevelopment (Shannon et al., 2018; Tong et al., 2015) (reviewed in Fame and Lehtinen, 2020). Thus, the ChP could provide insights into disease pathology and provide potential therapeutic targets for a wide range of disorders.

Remarkably little is known about the molecular mechanisms governing these functions of the ChP, its cellular networks, and histology. Each ChP develops independently from distinct locations along the roofplate, where capillaries, mesenchymal and neural crest cells invaginate the neuroepithelium (Hunter and Dymecki, 2007; Lun et al., 2015a; Wilting and Christ, 1989). Bulk profiling of whole tissue (Liddelow et al., 2010; Lun et al., 2015b; Silva-Vargas et al., 2016) or sorted subpopulations (Lun et al., 2015b) indicates that each ChP retains a developmental blueprint of its origins along the body axis, with ventricle-specific transcriptomes and secretomes for the lateral and 4th ventricle ChPs (Lun et al., 2015a). The less-accessible third ventricle is the least explored, and boundaries of all ChPs with adjacent neural tissues remain poorly defined. Earlier efforts to address these deficiencies were limited by the lack of techniques to access, isolate, and comprehensively profile the ChP across brain ventricles and ages.

Here, we characterized the ChP across all brain ventricles in the developing, adult, and aging mouse brain, by single cell and single nucleus RNA-Seq (sc/snRNA-seq), and spatial mapping of specific RNAs and proteins. We profiled 15,620 cells and 83,040 nuclei, followed by multi-tiered validation with single molecule fluorescence *in situ* hybridization (smFISH), immunostaining, and transgenic lines. We used whole tissue imaging to map the identified cell types, sub-types and states to uncover specialized niches within ChPs and along transition areas between the ChP and adjacent brain parenchyma. Trajectory inference of developing ChP cells predicted a common progenitor pool for epithelial and neuronal cells, which we validated by fluorescent tagging and lineage tracing. While some expression signatures were invariant across ages and ventricles, such as the expression of the SARS-CoV-2 receptor *ACE2* in mesenchymal and epithelial cells, others shifted with age or by ventricle, especially for epithelial and fibroblast cells. Ligand-receptor expression patterns across cell types predicted age- and ventricle- specific cell-cell interactions within the ChP, with a previously unappreciated role for mesenchymal cells (fibroblasts and pericytes) in the inferred cellular crosstalk, and an enhancement of IL-1β signaling from resident macrophage cells to endothelial and mesenchymal cells with age. Our molecular, cellular and spatial map of the ChP will be a resource for creating tools to access and control this essential brain-body barrier.

RESULTS

Molecular survey defines the cellular composition of the ChP across ventricles and ages

To chart a cell atlas of the developing, mature, and aging ChP, we profiled 15,620 single cells (scRNA-seq) and 83,040 single nuclei (snRNA-seq) from the lateral (LV), third (3V), and fourth (4V) brain ventricles of developing (embryonic day [E]16.5, n = 13), adult (4 months, n = 4) and aging (20 months, n = 9) mice (Figure 1A-C, F-H). We refined microdissection, cell dissociation and nucleus isolation techniques to obtain healthy single cells and nuclei from all ChPs (Figure 1A, STAR Methods). We conducted scRNA-seq for embryonic samples and snRNA-seq for all ages (Figure 1B, STAR Methods) (Gaublomme et al., 2019; Habib et al., 2017).

Embryonic cells partitioned into clusters identifying epithelial, mesenchymal (mural and fibroblast), endothelial, immune, neuronal and glial cells in each ChP from all ventricles (by

marker genes expression, Figure 1C, S1A,B,C, Table S1, STAR Methods). We determined the spatial positions of each major cell type within the ChP tissue from each ventricle by immunostaining of marker genes in whole explants and tissue slices of the developing brain (Figure 1D,E). Notably, actively cycling cell subsets were present within each of the six major cell classes in the developing ChP (Figure S1D) and were enriched along the base of the ChP proximal to the brain (Figure S1E).

SnRNA-seq of embryonic, adult, and aged ChP identified the same major cell classes in each ventricle (as in scRNA-seq of embryonic samples, Figure 1F), with conservation of overall cellular composition with age. While tissue maturation was accompanied by a distinct shift in gene expression between embryo and adult/aged ChP (Figure 1F-H, S1F,G), canonical cell-type markers were conserved across ages and ventricles (Figure 1I, Figure S1H,I).

Neuronal and glial cell populations in the ChP

We captured neuronal (*Tubb3* expressing) and glia-like (*Slc1a3*/EAAT1 or GFAP expressing) cells in the ChP across all ages, validated by immunostaining (Figures 1C,D,I, S1J-L), in agreement with previous studies (Lindvall et al., 1978). The neuro-glial populations were proportionally low (8%/2.5% of cells/nuclei, Figure S1B,G), yet sub-clustering revealed substantial diversity within each population.

In embryos, subsets of glial cells expressed markers of neural progenitor/stem-like cells (e.g. *Pax6, Nes, Sox2, Rspo2/3*) or of oligodendrocyte precursor cells (OPCs, e.g. *Olig1, Olig2*) (Kriegstein and Alvarez-Buylla, 2009) (Figure 2A, S2A,B). Subsets of neurons expressed markers of intermediate progenitors (e.g. *Eomes/Tbr2*) or of immature neurons (e.g. *Neurod1/2, Dlx1/2*), and various neuropeptides (e.g. *Vgf, Chgb*) (Figure S2B).

Two neuro-glial subsets in the 3V expressed markers of developing pinealocytes (e.g. *Crx, Krt19*; Figure 2A, clusters 12 and 13, Figure S2B), which develop caudal to the 3V ChP. We leveraged the inclusion of adjacent brain tissue in our atlas to map the boundary between the 3V ChP and developing pineal gland using published ISH (Lein et al., 2007; Visel et al., 2004) of marker genes from our data (Figure S2C). The diversity of embryonic glia and neuronal populations observed in scRNA-seq was confirmed by snRNA-seq and expanded to adult and aged ChP (Figure S2D,E) (Dulken et al., 2017; Mizrak et al., 2019; Shah et al., 2018).

An inferred common progenitor pool for epithelial and neural cells validated by lineage tracing

The embryonic ChP scRNA-seq profiles of epithelial, glial, and neuronal cells were not discretely separable by low-dimensional embedding (Figure 1C, STAR Methods), suggesting a common progenitor pool for both epithelial and neuronal cells may exist in the ChP. We thus modeled the predicted continuum between glial, neuronal, and epithelial cells using a diffusion map (Haghverdi et al., 2016) of 3V ChP cells (Figure S1D). The analysis arranged neurons and mature epithelial cells at two opposite ends of a trajectory, with a progenitor glia-like population at the node between them (Figure 2B, further supported RNA velocity (La Manno et al., 2018) analysis, Figure S2F).

The predicted progenitors expressed proliferation (*Mki67*) and known markers (*Pax6, Rspo2/3, Wnt5a/3a/1, Fabp7,* clusters 7 and 8 in Figure 2A,B S2B; STAR Methods), previously reported for precursors of ependymal cells and cortical neurons (Kriegstein and Alvarez-Buylla, 2009), with *Wnt1* having the most specific expression (Figure S2G). *Wnt1* mutant mice have disrupted 3V and 4V ChP formation (Louvi and Wassef, 2000). *Wnt1* contributes to lower rhombic lip (LRL)-derived 4V ChP (Awatramani et al., 2003; Hunter and Dymecki, 2007), but the upper rhombic lip (URL) *Wnt1* progenitor pool contributes largely to cerebellar development (Wingate, 2001) and expression was noted in the ChP (Hagan and Zervas, 2012). Focusing on the URL, we validated that *Wnt1*+ cells localized near *FoxJ1*-expressing ChP epithelial cells (by smFISH and immunohistochemistry, Figures 2C-G).

We confirmed our hypothesis of a common progenitor pool by lineage tracing the progeny of *Wnt1+* progenitors (by crossing *Wnt1-CRE2* (Lewis et al., 2013) with *R26R-Confetti* mice (Livet et al., 2007; Snippert et al., 2010), Figure 2H,I. *Wnt1*-derived epithelial cells in the maturing 4V ChP extended away from the URL, and *Wnt1*-derived neurons were in close proximity to progenitors in the URL (Figure 2J,K). These data support our model of a common progenitor pool that can give rise to both cell types. Analysis of 3V ChP in *Wnt1-CRE2::R26R-Confetti* mice further revealed *Wnt1*-lineage contributions to 3V ChP epithelial cells (Figure 2L).

Differentiating epithelial cells had distinct spatial organization and ciliogenesis expression programs. The maturing ChP epithelial cells in each ventricle transiently expressed ciliogenesis genes including *Ccdc67/Deup1* (Figures 2B, M-O), which drives centriole biogenesis, an essential step of multi-ciliation (Brooks and Wallingford, 2014). *Shisa8*, a reprogramming regulator (Schiebinger et al., 2019), was also expressed near the base of acetylated tubulin tufts in multi-ciliated epithelial cells (Figure 2N,O). We mapped the differentiating populations to distinct spatial boundaries within each ventricle (Figure 2P-R), with progenitor cells located near the ChP-brain boundary (by smFISH of *Rspo1/2/3; Wnt2b/3a/5a; Axin2*) (Figure S2H-K). Notably, the proportion of replicating epithelial cells was reduced from ~10% in embryonic ChP to ~1% in adult ChP, with an overall shift towards more mature cells compared to ciliogenic epithelial cells (p-value < 0.05, t-test on fraction of cells, Figure S2L). This maturation gradient of embryonic ChP epithelial cells matches prior models (Liddelow et al., 2010; Shuangshoti and Netsky, 1966) and provides a molecular handle for investigating distinct stages of epithelial cell development.

Epithelial cell programs are regionalized across brain ventricles in all ages

We next examined each of the major differentiated ChP cell populations – epithelial, mesenchymal, immune and endothelial. In each case, we first analyzed the embryonic cells (profiled by scRNA-seq) across the three ventricles, and then compared developing, adult, and aged mice (as profiled by snRNA-seq). Together these analyses identified shared and regionalized gene programs and distinguished those that are age-invariant and age-dependent.

In the embryo, epithelial cells formed the largest cell class in each ChP (by scRNA-seq, Figure S1B) and partitioned into subsets representing cycling, newly differentiated cells

undergoing ciliogenesis (above, Figure 2N), and mature cells (Figure 3A). Mature epithelial cell profiles partitioned by ventricle (Figure 3A), matching differential gene expression between LV and 4V ChP by bulk RNA-seq (Lun et al., 2015b) (Figure S3A). To identify ventricle-specific expression programs of embryonic epithelial cells, we performed topic modeling (Bielecki et al., 2021; Blei et al., 2003; Dey et al., 2017; Pritchard et al., 2000) (STAR Methods), to learn expression programs ("topics") and model cells as a mixture of topics. Briefly, a gene can belong to multiple topics with different weights, reflecting the gene's role in each topic; and a topic's weight for a given cell reflects the relative prominence of the expression program in that cell. We learned a topic model across all embryonic epithelial cells in the scRNA-seq dataset, and searched for topics that were differentially weighted in a subset of cells or enriched for genes of a specific biological process (Figure 3B, S3B,C STAR Methods, Table S2), such as ciliogenesis and immediate early genes (Figure S3B,C,D, Star Methods). Immediate early gene expression (Topic 19, Figure S3B,C) may reflect a response to tissue dissociation (van den Brink et al., 2017) as it was reduced in single nucleus profiles (Lacar et al., 2016) (Figure S3D).

Several topics reflected cross-ventricle regionalized gene programs (Topics 3, 6, 11, 14, 16, and 23), having differential weights between cells from different ventricles (Figure 3B, S3C). We validated the ventricle-specific enrichment of key topic-associated genes using smFISH and in published data (Visel et al., 2004) (Figure 3C,D). For example, *Ins2*, encoding an insulin precursor and associated with Topic 16, was over-expressed in 3V epithelial cells in the embryo (in scRNA-seq data, Figure 3B-D). Regionalized differences identified by scRNA-seq data (Figure 3C) were recapitulated in the corresponding embryo snRNA-seq data (Figure S3E). For example, *Ins2* was expressed in the 3V ChP, supporting the model that the ChP is an internal source of insulin for the brain (Mazucanti et al., 2019).

Other topics reflected spatial expression patterns within a ventricle. For example, epithelial cells in the ChP partitioned into two subpopulations by their weights of topics 6, 11 or 23 (Figure 3B,E, S3F). While these topics were highest in 4V, they also showed intra-ventricle variation in epithelial cells in other ventricles (Figure 3B). Mapping the expression of highly scoring genes for these topics in the 4V ChP *in situ* identified a rostro-caudal gradient of expression (Figure 3E), which may derive from the earliest stages of development, when roof plate progenitors originating from distinct rhombomeres give rise to hindbrain and 4V ChP (Hunter and Dymecki, 2007).

Comparing patterns across three age groups profiled by snRNA-seq, we found both age-invariant and age-dependent expression patterns, including regionalized patterns, with the main shift occurring from embryo to adult and then persisting into aging (Figure 3F,G). We found age-dependent expression of transporters and channels involved in ion and water movement across the epithelium, aligning with a key function of epithelial cells to produce CSF (Damkier et al., 2013; Fame and Lehtinen, 2020). For example, in adult ChP *Slc12a2* (NKCC1), *Kcnj13* (Kir7.1), and *Slc4a5* (NBC4) were upregulated (see also (Xu et al., 2021)), while *Aqp1* was modestly downregulated (Figure 3H, S3G). There were also age-dependent expression of genes encoding secreted proteins (Figure 3H, S3H, Table S3), including the "anti-aging" gene *Klotho* (Kuro-o et al., 1997; Zhu et al., 2018), which increased with age (Figure 3H).

Across all ages, differentially expressed genes were partitioned into three groups by age- and ventricle-dependent expression: First, age-invariant ventricle-dependent genes (*e.g., Wls* in 4V, *Emx2* in LV, Figure 3I, Table S3); Second, age- and ventricle-dependent genes (*e.g., Rspo3* in 3V, Figure 3J, Table S3), including a gene subset regionalized in adult and aged mice that were either not yet detected or not regionalized in the embryo at E16.5 (Figure S3I,J). Third, age-dependent and ventricle-invariant genes changed with age in all ventricles. These were enriched for specialized programs across ages: Embryonic epithelia upregulated genes for developmental processes (Figure 3K, S3K), while aged epithelia upregulated host-defense programs (Figure 3L, FDR q-value < 0.01, GOrilla (Eden et al., 2007, 2009;Baruch et al., 2014). Thus, epithelial cells likely adapt to fulfill age-dependent functions in the brain.

Mesenchymal cell programs are regionalized across brain ventricles

Mesenchymal cell profiles partitioned into fibroblasts and mural cells expressing pericyte and vascular smooth muscle cell (vSMC) markers (Figure 4A, S4A), consistent with cranial mesenchyme and neural crest contributions to the stromal space (Martik and Bronner, 2017; Wilting and Christ, 1989). Topic modeling of the embryonic cells recovered topics capturing mesenchymal cell types (*e.g.,* pericytes (topic 3), proliferating cells (topics 12 and 16)), and ventricle-dependent topics within fibroblasts (*e.g.,* LV (Topics 8 and 18), 3V (Topics 2 and 7) and 4V (Topic 5)) (Figure 4B, S4B,C, Table S4). We validated ventricle-dependent genes using published ISH data (Figure S4D, Visel et al., 2004). 3V ChP fibroblasts (Topic 7) shared expression signatures with meningeal fibroblasts (*e.g., Apod, Slc1a3*) and the 'ceiling cell' fibroblast subtype (*e.g., Crym,* Figure 4B, S4E; DeSisto et al., 2020). The ventricle-dependent topics revealed regionalized expression of genes encoding growth factors (*Bmp4/7, Wnt4/2*) and extracellular matrix proteins (Figure 4B, S4F). 4V ChP fibroblasts also expressed high levels of genes encoding signaling molecules with roles in hindbrain development (*e.g., Hhip* (Chuang and McMahon, 1999), *Ptch1* (Huang et al., 2009), *Rbp4* (Chang et al., 2016), and *Wisp1* (Lun et al., 2015a, Figure 4B, S4D).

Comparing patterns across the three age groups using snRNA-seq data revealed all mesenchymal cell types – pericytes, fibroblasts, vSMCs, and meningeal fibroblasts (Figure 4C-F, S4G). In fibroblasts, we found both age-invariant and age-dependent patterns, including regionalized patterns (Figure 4G,H, Table S5). As in epithelial cells, age-dependent fibroblast genes typically changed postnatally and were maintained in aged ChP (Figure 4H). Among age-dependent ventricle-invariant genes, embryonic fibroblasts expressed higher levels of developmental and morphogenesis genes, whereas the adult and aged fibroblasts upregulated transporters, receptors, peptidase and proteolytic activity genes (Figure 4I, S4H,I).

ACE2, the SARS-CoV-2 receptor is expressed by mesenchymal cells in the ChP

Mesenchymal cells across all ages and ventricles expressed *Ace2* (Angiotensin I converting enzyme 2; Figure 4J,S4J), the SARS-CoV-2 receptor, and other known and putative accessory components, including cathepsins *(Ctsl* and *Ctsb* (Muus et al., 2020)) and Neuropilin-1 (NRP1 (Cantuti-Castelvetri et al., 2020)) (Figure 4J, S4J). We validated ACE2 protein expression by mesenchymal cells in the stromal space (Figure 4K) and on some epithelial cells in embryonic, adult, and aged ChP (Figure 4K,L, S4K), similar to reports in

human ChP (Yang et al., 2020). We also validated the expression of NRP1 protein, an effector of SARS-CoV-2 cell entry and infectivity, in mesenchymal cells (Cantuti-Castelvetri et al., 2020) (Figure 4M). These data highlight the potential of mesenchymal and epithelial ChP cells to facilitate viral particle entry into the CSF (Pellegrini et al., 2020b, 2020a; Wu et al., 2020) in all ventricles and ages and to contribute to neurological sequelae associated with SARS-CoV-2 infection (Ellul et al., 2020).

Homeostatic macrophage diversity within ChP across ages

In the embryonic ChP, scRNA-seq profiles spanned eight subsets of immune cells: B cells, lymphocytes, macrophages, basophils, mast cells, dendritic cells, monocytes and neutrophils (Figure 5A,B), each expressing specific cytokine, chemokine, and complement component genes (Figure S5A,B).

In macrophages ($Cx3cr1^+$;$Csf1R^+$), the largest class of immune cells in the ChP, we found heterogeneity within stromal and CSF-contacting epiplexus cells. Diffusion map embedding of scRNA-seq embryonic profiles showed graded gene expression patterns spanning three transcriptional states (Figure 5C, STAR Methods). Differentially expressed genes between states included the hyaluronan receptor *Lyve1* (Jordão et al., 2019a; Lim et al., 2018); *Spp1*, a potential regulator of phagocytosis in the brain (Hammond et al., 2019); *Slc40a1*, an iron transporter; and *Spic*, which marks red pulp macrophages (Haldar et al., 2014) and bone marrow macrophages (Kohyama et al., 2009) that we confirmed by IHC (Figure 5C, S5C). A subset of *Slc40a1*$^+$ macrophages expressed *Spic* and *Clec4n* (Figure S5D), corresponding to recently described *Clec4n*$^+$ macrophages in postnatal ChP (Li et al., 2019). Macrophage states were associated with distinct spatial niches in the ChP, either basally under the epithelial cell monolayer or on the apical surface (*e.g.,* epiplexus position, Figure 5D), by image analysis of *Cx3cr1-GFP* transgenic mouse. *Cx3cr1-GFP*-expressing cells tiled across the ChP (Figure 5E; Cui et al., 2020), with the subset expressing *SLC40A1* located proximal to major vessels, suggesting roles in regulating iron homeostasis (Figure 5F). A subset of the $Cx3cr1^+$ macrophages located on the apical ChP surface expressed LYVE1 (Figure 5G).

SnRNA-seq of embryonic, adult, and aged ChP across all ventricles identified macrophages, neutrophils, dendritic cells, plasma cells, and lymphoid (B- and T-) cells (Figure 5H, S5E,F). Macrophages were the most prevalent and were associated with blood vessels across all ages (Figure S5G; Shipley et al., 2020). The macrophages expressed markers of border associated macrophages (BAMs) (e.g., *Apoe, Ms4a7, Ms4a6c*) recently identified in periluminal regions, meninges, and ChP (Van Hove et al., 2019). In agreement with recent reports (Van Hove et al., 2019), we found diversity within the BAMs, which segregated into two subsets defined as major histocompatibility complex (MHC) class II^{low} and MHC II^{high}. However, in contrast to Van Hove et al., our data revealed that this separation was age-dependent and potentially represented a maturation-dependent shift from MHC II^{low} to MHC II^{high} (Figure 5I, S5I,J, Table S6). For example, CD206 (*Mrc1*, mannose receptor C-type I) expressed by embryonic macrophages was downregulated in adults, whereas CD74 (MHC class II associated protein) was upregulated in adult and aged macrophages *vs.* embryos (Figure 5J-L, Figure S5H). Similarly, we found a subset of macrophages expressing markers previously

defined as subdural-specific BAMs (e.g., *Lyve1, Ednrb, Colec12*; Van Hove et al., 2019) that were enriched in embryonic ChP macrophages in our dataset (Figure S5H).

Arterio-venous zonation and blood brain barrier protein expression in ChP vasculature

The ChP serves as an important blood-CSF barrier. While the major vessels that feed each ChP are well described (Lun et al., 2015a), the identity, structure and development of vascular cell types within the ChP remain largely unknown. In the embryo, topic modeling of scRNA-seq data of vascular cells recovered expression programs associated with capillary (Topic 3), arterial (Topic 8 and 10) and blood-brain barrier (BBB)-associated (Topic 11) cells (Figure 6A, S6A,B, Table S7). We spatially mapped the developing arterio-venous zonation in the embryonic LV ChP in whole explants by combining the pan-endothelial marker PECAM1 with markers for arteries (*Acta2+, Vwf+)* and veins (*Acta2–, Vwf+*) (Vanlandewijck et al., 2018). Histological analyses revealed arteries developing obliquely across the ChP and veins running along the ventricular free margin of the tissue (Figure 6B). The arterio-venous zonation in the developing embryo was accompanied by enriched capillary marker expression (e.g. *Esm1*) along the ventricular margin of the ChP, suggesting zonated gene expression in vessels across the developing ChP (Figure 6C).

Comparing single nucleus profiles across ages revealed that arterial, venous, and capillary identities were established across adult ages and ventricles (Figure 6D, S6C). In adult and aged LV ChP, IHC showed that arteries and veins were regularly segmented across the tissue (Figure 6E,F; Shipley et al., 2020) and connected by an expanded capillary-like network (Figure S6D) similar to human tissue (Hudson, 1960). Moreover, *Plvap*, which marks diaphragms of fenestrated endothelial cells (Herrnberger et al., 2012), scored highly in Topic 3 from scRNA-seq of embryonic cells (Figure 6A), and was also identified in adult and aged snRNA-seq profiles (Figure S6C). These findings match prior reports detailing the appearance of fenestrae during early embryonic rodent development (Figure S6E), which increase in number as the ChP matures (Keep and Jones, 1990). While we did not observe overt regionalization of endothelial cell programs, venous markers were enriched in the 3V ChP across all ages (Figure 6D, S6F,G), likely resulting from capture of the proximal vein of Galen (Mancini et al., 2015) (Figure S6H). The stereotyped vascular organization was retained in aged ChP (Figure 6F), where *Vwf* and *Selp (P-selectin)* expression were also detected (Figure 6G). IHC revealed VWF and SELP colocalized to enlarged luminal domains of vessels in aged mice (Figure 6H), suggesting age-associated vascular damage. Overall, these results identify molecular identities and vascular organization of ChPs across ventricles and ages that match vascular patterning in the human ChP (Hudson, 1960).

Notably, topic modeling of embryonic ChP cells also uncovered a previously unknown brain barrier transition zone embedded in the molecular and vascular map of the ChP, which we validated across ages. Specifically, non-capillary endothelial cells in the embryonic ChP expressed BBB markers (*Cldn5* and *Mfsd2a*, Topic 11) (Figure 6A), even though the ChP is recognized to lack a classic BBB (Ben-Zvi et al., 2014; Saunders et al., 2018b). *Cldn5* expression persisted in a subset of endothelial cells in snRNA-seq from all ages (Figure 6I, S6C), and CLDN5 protein was prominent in the major arteries bifurcating from the choroidal artery and extending into the ChP (Figure 6J, K, S6I).

Ligand-receptor analysis identifies mesenchymal cells as an interaction hub across ages and ventricles

Analysis of cognate ligand-receptor expression patterns across cell types, ventricles and ages (STAR Methods) predicted extensive cellular crosstalk involving all major ChP cell types (Figure 7). Briefly, for each ventricle and age, we identified putative interactions between each of the 6 major cell types by the expression of a ligand and its cognate receptor (through the CellPhoneDB (Efremova et al., 2020), STAR Methods). We estimated the significance of individual interactions (Efremova et al., 2020), and of the number and nature of observed interactions, between pairs of cell types by permutation tests (STAR Methods). We found significant individual interactions between each pair of cell types across all ventricles and ages, with specific cell type pairs having a significant enrichment in the number of interactions (Figure 7A, S7A,B, Table S8). We then focused all subsequent analyses only on significant interactions.

The number of significant ligand-receptor interactions between each pair of cell types changed across ventricles and ages (Figure 7A, Figure S7A,B). Overall, mesenchymal and epithelial cells had a high number of interactions (Figure 7A, Figure S7B). The majority of significantly interacting cell type pairs involved mesenchymal cells (FDR<0.05, 60%, 70% and 85% in embryonic, adult and aged, respectively), followed by epithelial cells (FDR<0.05, 45%, 55% and 42% in embryonic, adult and aged, respectively). For example, mesenchymal cells (fibroblasts and pericytes) expressed *Pdgfra* and *Pdgfrb* respectively, and epithelial and endothelial cells expressed their cognate ligands, *Pdgfa and Pdgfb* respectively (Figure S7C). *Wnt5a*, a regulator of 4V ChP and hindbrain development (Kaiser et al., 2019), was most robustly expressed by mesenchymal cells and its receptor *Ror1* was expressed, amongst others, by epithelial cells, suggesting lifelong contributions to ChP function (Figure S7C). Other notable interactions included *Vegfa* in epithelial and mesenchymal cells and its receptor *Flt1* on endothelial cells (Figure S7C).

Notably, in a more conservative, degree-preserving permutation test, the number of predicted interactions between most cell type pairs was not statistically significant (Figure S7D), indicating the dominance of a cell type in the crosstalk across all cells and not specific pairs. In addition, there were some differences between predicted significant interactions from scRNA-seq *vs.* snRNA-seq for embryo ChP, which may reflect differences in cell type recovery between methods (Figure S7A).

Comparing significant interactions across ventricles or ages revealed age- or ventricle-dependent interactions and overall differences in the number of interactions (Figure 7B-D). For example, *Nov-Notch1* ligand receptor pair (LRP) expression in the 3V ChP and *Dlk1-Notch* LRP in 4V ChP predicted ventricle-specific signaling from mesenchymal cells to most other cell types (Figure 7C). In 3V and 4V ChP, *Bmp5-Bmpr1b* LRP expression predicted signaling from mesenchymal to neuro/glial and epithelial cells (Figure 7C). Among age-specific interactions, several LRPs were embryonically enriched. For example, *Rspo2-Lgr4* LRP expression predicted signaling mainly from neuro/glial cells to epithelial and neuro/glial cells in the LV ChP. *Lgr4* receptor is a key regulator of development and differentiation (Bell et al., 2008; Kinzel et al., 2014), consistent with our report of a common *Rspo2*+ progenitor for neurons and epithelial cells (Figure 2). Further, in the developing

ChP, *Efna5-Ephb2* LRP expression predicted signaling from epithelial cells to neuro/glial cells (Figure 7D), suggesting a role for Ephrin signaling in differentiation (similar to the gut; Kania and Klein, 2016). Finally, we predicted age-dependent signaling from mesenchymal, endothelial and epithelial cells expressing the insulin-like growth factor *Igf2* to various cells expressing its receptors, *Igf1r* and *Igf2r*, predominantly in embryonic ChP (Figure 7D, S7C), reinforcing the role of IGF signaling in development (Lehtinen et al., 2011). Among the ligand-receptor pairs expressed in adult that increased with age, *Cxcl12-Ackr3* LRP expression predicted signaling from mesenchymal to endothelial and other cell types (Figure 7D).

Enhanced putative IL-1β signaling between macrophages, endothelial and mesenchymal cells in aging

Several interactions were predicted across all ventricles and ages, between immune cells and structural cells (epithelial, mesenchymal and endothelial), in line with the diverse functions assigned to immune cells in other barrier systems (Krausgruber et al., 2020). For example, *Csf1*, a signal for macrophage and monocyte differentiation was expressed by mesenchymal cells and endothelial cells, suggesting that myeloid cell signaling maturation for *Csf1r* expressing cells exists in the ChP throughout life (Figure S7C, Table S7).

Consistent with previous reports of overall induction of inflammatory signaling in the aged ChP (Baruch et al., 2014; Paré et al., 2018), IL-1β expression was induced in aged ChP macrophages and its receptor, IL1R1, was enriched in endothelial and mesenchymal cells (Figure 7E). We validated this observation, finding that IL-1β immunolabeled macrophages in the aged ChP localized to vessel-like structures bridging the ChP with the brain parenchyma (Figure 7F). Its cognate receptor, IL1R1, was expressed by endothelial, mesenchymal and epithelial cells, and IHC revealed enrichment along endothelial structures (Figure 7G). Overall, these interactions may contribute to age-dependent macrophage migration and infiltration of the ChP brain immune barrier.

DISCUSSION

The lack of a detailed cellular and molecular map for the ChP has been a major obstacle to elucidating its roles in instructing brain development, brain function, understanding its barrier properties, and unlocking its lifelong therapeutic potential. Here, we characterized ChP cell types across ventricles and ages, uncovered ventricle- and age-specific gene expression programs for epithelial and mesenchymal cells, described immune cell diversity, mapped developing and aging vascular structures, and uncovered age-dependent changes within ChP cellular signaling networks.

Our work builds on previous findings (Lun et al., 2015a) to demonstrate the ventricle-specific regionalization of epithelial and mesenchymal cells. Ventricle-specific identities were maintained in the adult and aged tissue, but additional genes became regionalized in the adult (and persisted into aging), either by activation of expression (for genes not expressed in the embryo) or by restriction of expression (for genes expressed across ventricles in the embryo). Gene programs and graded expression patterns, particularly across

4V ChP epithelial cells, may arise from the segmental development of the 4V ChP from distinct rhombomeres (Awatramani et al., 2003; Hunter and Dymecki, 2007).

The ChP is considered to be a primary producer of CSF and CSF-distributed factors (Ghersi-Egea et al., 2018; Lun et al., 2015a; Saunders et al., 2018b), and our cell atlas provides an opportunity to identify specifically which cells contribute. Essentially all major ChP cell types, and in particular ChP fibroblasts, also expressed many secreted factors found in CSF, including *Igf2* (Lehtinen et al., 2011). Notably, mesenchymal cells were the cell type with the most predicted interactions with other ChP cell types. Future studies will determine if secreted factors of non-epithelial origin are restricted to targets within the ChP stromal space, or whether transport mechanisms allow them to contribute to CSF-based signaling in the brain.

Our profiles of ChP immune cell populations revealed spatial organization and age-dependent expression across ventricles and within the ChP. Most ChP macrophages shared signature genes recently described for adult ChP macrophages (Jordão et al., 2019a) and were *Sall1* negative (Hammond et al., 2019). While we did not uncover a transcriptional signature purely for epiplexus cells, in validation experiments of *Lyve1* expressing *Cx3cr1*-positive cells, we observed that some, but not all, epiplexus cells expressed LYVE1, demonstrating heterogeneity in immune cells positioned on the ChP surface. We noted age-dependent gene expression patterns in macrophages, such that genes upregulated during development, such as *Cd206/Mrc1*, were downregulated in adult and aged macrophages. Conversely, adult macrophages upregulated *CD74*, a chaperone of antigen presentation protein that was even further upregulated in the aged ChP. These maturation dependent changes agree with a recent report of BAMs (Van Hove et al., 2019). However, our data further clarify that this diversity is likely maturation-dependent, suggesting that the previously described diversity reflect instead a transition state between embryo and adult. Overall, we observed an upregulation of the inflammatory signals in the aged ChP in agreement with prior studies (Baruch et al., 2014) that was reflected in expression of *Ifit1* and *Il1b* in aged epithelial cells. An improved understanding of ChP resident immune cells will facilitate future studies aimed at testing the protective and/or damaging consequences of ChP inflammation on brain function.

In summary, our study provides a comprehensive map of the molecular, cellular and spatial diversity of each ChP of the developing, adult, and aging mouse brain. Since the ChP-CSF system is implicated in a growing number of neurologic conditions, our dataset offers molecular insight that should accelerate future studies investigating the lifelong, active regulation of the ChP brain-body barrier.

Limitations of the study

To generate the atlas we overcame several challenges, while encountering new limitations. (1) To overcome the small tissue size, we isolated sufficient numbers of cells by pooling samples across donors. This approach was particularly salient for immune cells, which may nonetheless benefit from further enrichment for greater in-depth analysis. (2) We endeavored to isolate pure ChP by dissecting along anatomically defined tissue boundaries, which were at times limited (e.g., 3V ChP that has less defined borders). (3) We dissociated cells at

different ages for whole cell sequencing. However, cellular health was particularly challenging for adult and aged tissues, ultimately leading us to favor differential sample processing (e.g., scRNA-seq for embryonic vs. frozen samples and snRNA-seq for adult/ aged also applied to embryonic). This strategy subsequently introduced additional computational challenges in comparison of the two datasets. (4) Transitions between cell states and ages are continuous and required adjustments to our computational tools including the use of topic modeling. (5) We cannot rule out the possibility that we may miss some lower expressed genes of interest to ChP biology due to the limitations in depth of coverage.

STAR METHODS

RESOURCE AVAILABILITY

Lead contact—Further information and requests for resources and reagents should be directed to and will be fulfilled by the Lead Contact, Maria K. Lehtinen, maria.lehtinen@childrens.harvard.edu.

Materials Availability—No new reagents generated.

Data and Code Availability—Raw and processed mouse sequencing data is available at https://portals.broadinstitute.org/single_cell and at the Gene Expression Omnbius (GEO) database GSE168704.

EXPERIMENTAL MODEL AND SUBJECT DETAILS

Animal models—All mouse work was performed in accordance with the Institutional Animal Care and Use Committees (IACUC) and relevant guidelines of Boston Children's Hospital and Masaryk University.

Embryonic day (E) 16.5 embryos were obtained from time-pregnant CD-1 dams for embryonic scRNA-seq analyses. For snRNA-seq analyses, E16.5 embryos, adult (4 months) and aged (20 months) C57BL/6J males and females were used. All animals were housed under 12hr/12hr day night cycle with access to standard chow and water ad libitum.

CD1(ICR)– Charles River Laboratories Strain 022.

Cx3cr1-GFP (catalog #: 005582, The Jackson Laboratory)

C57BL/6 – Charles River Laboratories

C57BL/6J – (catalog #: 000664, The Jackson Laboratory)

Wnt1-Cre2 – (catalog #: 002137, The Jackson Laboratory)

R26R-Confetti – (catalog #: 013731, The Jackson Laboratory)

METHOD DETAILS

ChP tissue dissection—Whole ChP tissues from embryonic and adult were isolated as follows. <u>LV ChP</u>: Cerebral cortical hemispheres were separated. Following incisions into the

cortical tissue at either end of the hippocampus, the hippocampus was rolled out using the flat surface of a microscalpel and the underlying LV ChP was separated from the hippocampus/fornix. <u>3V ChP</u>: The dorsal midline of the midbrain was exposed and 3V ChP was isolated. Specific to adult brain, flushing the midline region with 1xHBSS helped visualize the ChP, which was identifiable by a blood vessel running along its rostro-caudal axis. The adult 3V ChP extends ventrally and rostrally, ultimately connecting to the ventral base of the LV ChP. <u>4V ChP</u>: Hindbrain was separated from the brain. The cisterna magna was exposed by gently guiding away the developing or mature cerebellum to expose the 4V ChP.

FACS purification of healthy embryonic cells—LV, 3V and 4V ChP of three litters of embryonic E16.5 embryos were rapidly dissected and pooled together in dissecting medium (HBSS+0.6% Glucose+1xPen/Strep+Filtered medium 0.22 filter) (Corning, Cat:21-023-CV) + glucose (Sigma, Cat:7021-100G). Dissected ChPs were spun down at 300xG for 3 min. in a centrifuge at 4°C. Whole ChP was dissociated enzymatically by preparing fresh solution of collagenase II (Gibco, 17101-015) supplemented with 3 mM calcium (Sigma, C3881). Next, CP was tapped and flicked 30 times and incubated at 37°C incubator 3 consecutive times every 5 minutes over 15 minutes. The enzymatic solution with digested ChP tissue was then diluted using 1xHBSS, followed by pelleting down cells at 300xG for 3 mins at 4°C. TrypLE (Life Technologies, TrypLE, Catalog: 12604) was then added and samples were incubated for 5 min at 37°C followed by trituration using a micropipette. Samples were finally washed with ChP epithelial cell (CPEC) medium (DMEM+10%FBS+1xPen/strep) and resuspended in 1xHBSS + glucose + LIVE/DEAD staining kit (ThermoFisher, Catalog: L-3; 224). Live cells identified by green fluorescence (calcein-AM) (LifeTechnologies, Catalog L3224A) and lack of EtD-1 homodimer staining (L3224B) were selected and sorted by a MoFlo Astrios cell sorter (Beckman Coulter) into 500 μl filled into dissecting medium.

Single cell RNA-seq—Single cells were processed through the 10X Genomics Single Cell 3' platform using the Chromium Single Cell 3′ Library & Gel Bead Kit V1 and V2 kit (10X Genomics), as per the manufacturer's protocol. Briefly, 7,000 cells were loaded on each channel and partitioned into Gel Beads in Emulsion in the Chromium instrument where cell lysis and barcoding occur. This step was followed by amplification, fragmentation, adaptor ligation, and index library PCR. Libraries were sequenced on an Illumina HiSeqX at a read length of 98 base pairs.

Single nucleus RNA-seq—Tissues were minced in 50 μl of CST lysis buffer [10 mM Tris, 146 mM NaCl, 1 mM $CaCl_2$, 21 mM $MgCl_2$, 0.1% CHAPS, 40 U/mL of RNAse inhibitor] in an eppendorf tube for 10 minutes. Volume in the tube was raised by addition of 1 mL CST lysis buffer and then transferred to a 15 mL conical tube on ice. The eppendorf tube was rinsed with 1 mL CST lysis buffer and the volume was added to the 15 mL conical tube. The nuclei suspension was diluted to 5 mL with ST buffer [10 mM Tris, 146 mM NaCl, 1 mM $CaCl_2$, 21 mM $MgCl_2$, 40 U/mL of RNAse inhibitor] and filtered through a 20 μm filter into a 15 mL conical tube prior to centrifugation at 500G for 5 minutes at 4°C in a swing bucket centrifuge. Nuclei pellets were then resuspended in ST [10 mM Tris; 146 mM NaCl; 1mM $CaCl_2$; 21 mM $MgCl_2$; 40U/mL of RNase Inhibitor] for a final volume of ~100

μl. Samples were normalized, pooled and filtered prior to loading 10X at a total of 10,000 nuclei per channel, which were run on the 10X Single Cell RNA-Seq Platform using the Chromium Single Cell 3' Reagent Kits v3. Libraries were made following the manufacturer's protocol. Briefly, single nuclei were partitioned into nanoliter scale Gel Bead-In-EMulsion (GEMs) in the Chromium controller instrument where cDNA share a common 10X barcode from the bead. Amplified cDNA was measured by Qubit HS DNA assay (Thermo Fisher Scientific: Q32851) and quality assessed by BioAnalyzer (Agilent: 5067-4626). This Whole Transcriptome Amplified (WTA) material was processed through 3' V3 library construction, and resulting libraries were quantified again by Qubit and BioAnalzyer. Libraries from 4 channels were pooled and sequenced on 1 lane of Illumina HiSeqX by the Broad's Genomics Platform, for a target coverage of around 1 million reads per channel.

Tissue fixation and processing—Dissected ChP were fixed in 4% paraformaldehyde (in 1X phosphate-buffered saline, pH 7.4). For microtome sectioning, embryonic brains were drop fixed in 4% paraformaldehyde, and incubated in the following series of solutions in 1X phosphate-buffered saline: 10% sucrose, 20% sucrose, 30% sucrose, 1:1 mixture of 30% sucrose and Optimal Cutting Temperature (OCT) compound (overnight) and finally in OCT compound alone (1 hour). Samples were then frozen in OCT compound.

Immunohistochemical analysis—Cryosections were permeabilized with 0.1% Triton X-100 in phosphate-buffered saline, incubated with primary antibodies overnight, and incubated with secondary antibodies for 2 hours. Sections were counterstained with Hoechst 33342 (Thermo Fisher Scientific) and mounted on slides using Fluoromount-G (SouthernBiotech, Birmingham, AL).

For Ki67 staining, an antigen retrieval step was included: A food steamer (catalog number 5712, Oster, Boca Raton, FL) was filled with water and preheated until the chamber temperature reached 100°C; sections were then immersed in boiling citric acid buffer (10 mmol/L sodium citrate, 0.05% Tween 20, pH 6) and placed in the steamer for 20 min. Sections were then cooled to room temperature.

Antibodies and probes—We used the following antibodies: Rabbit anti-5-HT (1:3000, S5545, Sigma), Mouse anti-AQP1 (1:100, sc-32737, Santa Cruz), Goat anti-ACE2 (1:250, AF3437, R&D Systems), Mouse anti-ACTA2-Cy3 (1:200, C6198, Sigma); Rabbit anti-CCDC67 (1:500, 24579-1-AP, Proteintech), Rat anti-CD74-488 (1:100, 151005, Biolegend), Rat anti-CD31/PECAM1 (1:200, 550274, BD Pharmingen), Goat anti-CD62P/P-Selectin (1:100, AF737, R&D Systems), Mouse anti-CLDN5-488 (1:400, 331588, Invitrogen), Rabbit anti-COL1A1 (1:250, AB34710, Abcam), Goat Anti-ESM1 (1:250, AF1999, R&D Systems), Chicken anti-GFP (1:250, ab13970, Abcam), Rabbit anti-GFAP (1: 250, Z0334, Dako), Hamster anti-IL1B (1:100, 503513, Biolegend), Goat anti-IL1R1 (1: 200, AF771, R&D Systems), Rabbit anti-IBA1 (1:250, 019-19741, Wako), Mouse anti-KI67 (1:50, 550609, BD Pharmingen), Rat anti-KI67 (1:250, 14-5698-80, ThermoFisher), Goat anti-LYVE1 (1:300, AF2125, R&D Systems), Rabbit anti-MRC1/CD206 (1:250, ab64693, Abcam), Goat anti-NRP1 (1:250, AF566, R&D Systems), Rabbit anti-PAX6 (1:500, ab2237, Millipore), Rat anti-SPI1/PU.1 (1:250, MAB7124-SP, Novus), Rabbit anti-SPIC (1:35,

PA5-67537, ThermoFisher), Rabbit anti-SHISA8 (1:500, ab188621, Abcam), Rabbit anti-SLC40A1 (1:250, MTP11-A, Alpha Diagnostic International), Mouse anti-TUBB3 (1:100, 801202, Biolegend), Mouse anti-Acetylated Tubulin (1:250, T6793, Sigma), Rabbit anti-VWF (1:200, MA5-14029, ThermoFisher), Rat anti-WNT5A (1:250, MAB645, R&D Systems). Mouse anti-ZO1 (1:100, 33-9100, ThermoFisher).

We used the following RNAscope probes: *Axin2* (mm-Axin2-C3, Ref: 400331-C3), *FoxJ1* (mm-FoxJ1, Ref: 317091), *Ins2* (mm-Ins2-C2, Ref: 310751-C2), *Rspo1* (mm-Rspo1, Ref: 401991), *Rspo2* (mm-Rspo2, Ref: 402001-C2), *Rspo3* (mm-Rspo1, Ref: 402011-C3), *Wnt1* (mm-Wnt1, Ref: 401091), *Wnt2b* (mm-Wnt2b-C2, Ref: 405031-C2), *Wnt3a* (mm-Wnt3a, Ref: 405041), *Wnt5a* (mm-Wnt5a-C3, Ref: 316791-C3),.

Whole explant and cortical section RNAscope *in situ* hybridization and immunohistochemistry—LV, 3V, and 4V ChP explants were dissected at E16.5 and fixed with 4% paraformaldehyde (PFA) for 10 min. at room temperature (RT) in a 9-well glass plate before beginning the manufacturer's provided protocol for RNAscope Fluorescent Multiplex (ACD). Free-floating explants were incubated with Target Retrieval Reagent (ACD) in a steamer for 12 min. Subsequently, explants were washed 3x3 min. in double distilled water prior to incubation with Protease III Reagent (ACD) for 8 min. at 40°C, followed by another 3x3 min. wash cycle in double distilled water. Target Probes (ACD) were then hybridized and amplified according to the manufacturer's specifications. Following hybridization, immunohistochemical staining was performed in a subset of explants and described above. For RNAscope and IHC of cortical sections used in confetti experiments, 14 μm cryosections were prepared. After isolation, embryos were immediately transferred and kept in fresh 4% PFA for 2 hours, washed briefly in ice cold PBS, incubated overnight in 30% sucrose solution, and frozen at −80°C. Transcripts were detected using the RNAscope 2.0 assay for fresh frozen tissue (Advanced Cell Diagnostics). Probes were designed and provided by Advanced Cell Diagnostics, Inc. Staining was performed using the RNAscope protocol according to the manufacturer's instructions for fresh frozen sections processing (Wang et al., 2012, Kaiser et al., 2019). For immunostaining in confetti experiments, all sections underwent antigen retrieval by short boiling in the microwave followed by 15 min. incubation in 86°C pre-warmed water bath using antigen retrieval solution. Sections were washed in PBT (PBS with 0,5% Tween-20) and blocked in PBTA (PBS, 5% donkey serum, 0,3% Triton X-100, 1% BSA). Samples were incubated overnight at 4°C with primary antibodies diluted in PBTA. Following washes in PBT, samples were incubated with corresponding Alexa Fluor secondary antibodies for 1 hour at RT, followed by 5 min. incubation at RT with DAPI. Finally, samples were mounted and analyzed using Zeiss LSM 800 confocal microscope or Zeiss LSM 880 Airyscan for the analysis of the Confetti embryos. For the TUBB3 staining combined with *in situ* hybridization RNAscope analysis, the antigen retrieval step was excluded and the sections were washed using PBS followed by overnight incubation at 4°C with primary antibody in PBS containing 0.5% Triton X-100. Allen Brain Atlas (Lein et al., 2007) and Genepaint (Visel et al., 2004) were used to obtain *in situ* hybridization images of transcript localization within embryonic and adult brains.

Transmission electron microscopy—LV ChP was micro-dissected in HBSS (Thermo Fisher Scientific) and drop-fixed immediately in FGP fixative (5% Glutaraldehyde, 2.5% Paraformaldehyde and 0.06% picric acid in 0.2 M sodium cacodylate buffer, pH 7.4). After 2 hours at RT, the tissue was washed in 0.1M cacodylate buffer and postfixed with 1% Osmiumtetroxide (OsO_4)/1.5% Potassiumferrocyanide ($KFeCN_6$) for 1 hour, washed twice in water, washed once in 50mM Maleate buffer pH 5.15 (MB), incubated in 1% uranyl acetate in MB for 1 hour followed by one wash in MB, 2 washes in water, and subsequent dehydration in alcohol (10 min each; 50%, 70%, 90%, 2x10 min 100%). The samples were then put in propyleneoxide for 1 hour and infiltrated ON in a 1:1 mixture of propyleneoxide and TAAB Epon (TAAB Laboratories Equipment Ltd, https://taab.co.uk). The following day, the samples were embedded in TAAB Epon and polymerized at 60°C for 48 hours. Ultrathin sections (about 80 nm) were cut on a Reichert Ultracut-S microtome, picked up on to copper grids stained with lead citrate. Images were acquired with a JEOL 1200EX transmission electron microscope, and recorded with an AMT 2k CCD camera (Biological Electron Microscopy Facility, Harvard Medical School).

Scanning electron microscopy—LV ChP was micro-dissected in HBSS (Thermo Fisher Scientific) and drop-fixed immediately in FGP fixative (5% Glutaraldehyde, 2.5% Paraformaldehyde and 0.06% picric acid in 0.2 M sodium cacodylate buffer, pH 7.4). Post-fixation was performed in 1% osmium tetroxide in 0.1M sodium cacodylate buffer for 1 hour. This step was followed by rinsing in 0.1M sodium cacodylate buffer 3 times 15 min. each. The samples were dehydrated in a graded series of ethanol to 100% and dried using a Tousimis PVT-3D critical point dryer (Tousimis Research Corp., Rockville, MD). The dried samples were then attached to sample mounts using double sided conductive carbon adhesive tabs and sputter coated with 5 nm of platinum with a Cressington 208HR sputter coater (Cressington Scientific Instruments, Walford, UK). SEM images were acquired on a Hitachi S-4800 FE-SEM (Hitachi Ltd., Tokyo, Japan).

Hematoxylin and Eosin (H&E) staining—Paraffin-embedded brains were sectioned to a thickness of 5 μm. The sections were deparaffinized in xylene and then rehydrated via successive incubations in 100% ethanol, 95% ethanol, and water. Sections were incubated in Gill 3 hematoxylin (Sigma Aldrich, St. Louis, MO) for 2 min., followed by a 5-second incubation in 0.5% ammonia water to increase the contrast of the hematoxylin stain. Next, sections were rinsed in water and incubated in 1% alcoholic eosin for 3 min. Finally, sections were dehydrated via successive incubations in 95% ethanol and 100% ethanol, and mounted using Permount (Thermo Fisher Scientific).

Regionalized proliferation in the LV ChP—Tissue was stained with KI67 and Hoechst and imaged using laser scanning confocal microscopy with tiling function (LSM 710, Zeiss). The tissue images were divided into three equal regions along the dorso-ventral: (1) brain-proximal, (2) -medial, and (3) -distal regions. Nuclei were identified by Hoechst staining and proliferating cells were identified by overlapped KI67 staining. Percent proliferating cells were counted in each region. A total of four independent explants were quantified. Multiple comparisons ANOVA was employed using statistical software package Graphpad PRISM. Data are represented as mean ± SEM. $P < 0.05$ was considered significant.

Pre-processing of droplet-based scRNA-seq—De-multiplexing, alignment to the mm10 transcriptome and unique molecular identifier (UMI)-collapsing were performed using the CellRanger toolkit from 10X Genomics (version 1.1.0 for the first batch of embryonic scRNA-seq, which used V1 chemistry, and version 2.0. for experiments in batch two and batch three, which used 10x Genomics V2 chemistry). For each cell, we quantified the number of genes for which at least one read was mapped, and then excluded all cells with fewer than 500 detected genes. Since the total number of UMI and genes detected varies across cell types (Figure S1A), we further excluded epithelial cells with fewer than 10,000 total UMI and mesenchymal cells with fewer than 6,000 total UMIs. Genes that were detected in less than 5 cells were excluded. Expression values $E_{i,j}$ for gene i in cell j were calculated by dividing UMI counts for gene i by the sum of the UMI counts in cell j, to normalize for differences in coverage, and then multiplying by 10,000 to create TPM-like values (TP10K), and finally computing $\log_2(\text{TP10K} + 1)$. Batch correction was performed for each cell type separately using ComBat as implemented in the R package *sva* (Leek et al., 2012), using the default parametric adjustment mode. The output was a corrected expression matrix, which was used as an input to further analysis.

Pre-processing of droplet-based snRNA-seq data—De-multiplexing, alignment to the mm10 transcriptome with retained intronic regions (mm10_premrna_v1.2.0) and UMI-collapsing were performed using the CellRanger toolkit (version 3.1.0, V3 chemistry) from 10X Genomics. To address ambient (background) RNA and other confounders we applied CellBender (Fleming et al., 2019) to each sample separately with expected number of nuclei ranging between ~4,500 and ~8,000, depending on the sample, 15,000 total droplets included for the analysis and 200 epochs. For each nucleus, we quantified the number of genes for which at least one read was mapped, and then excluded all nuclei with fewer than 500 detected genes, or 200 detected genes for immune cell nuclei. Furthermore, we excluded nuclei that had more than 10% of total UMI's mapped to mitochondrial genes. Genes that were detected in less than 10 nuclei were excluded. Expression values $E_{i,j}$ for gene i in nucleus j were calculated by dividing UMI counts for gene i by the sum of the UMI counts in nucleus j, to normalize for differences in coverage, and then multiplying by 10,000 to create TPM-like values (TP10K), and finally computing $\log_2(\text{TP10K} + 1)$.

Identifying variable genes—Selection of variable genes was performed by fitting a logistic regression model to the cellular detection fraction (often referred to as α), using the total number of UMIs per cell/nucleus as a predictor as in (Montoro et al., 2018). Outliers from this curve are genes that are expressed in a lower fraction of cells/nuclei than would be expected given the total number of UMIs mapping to that gene, that is, likely cell-type or state-specific genes. We used a threshold of deviance between <-0.15 and <-0.3. For the embryonic scRNA-seq data, if there were enough cells from all three batches, variable genes were calculated within each batch, and only the intersection of variable genes in each batch were taken for downstream analysis. This was the case when analyzing all cells (Figure 1C), and epithelial and mesenchymal cells. Batch was ignored for computing variable genes for immune, endothelial and neuro-/glia-like cells. Batch was ignored for all snRNA-Seq data. We restricted the expression matrix to this subset of variable genes and values were centered and scaled and capped at a z-score of 10.

Dimensionality reduction using PCA and visualization using t-SNE or UMAP—
We restricted the expression matrix to the subsets of variable genes and high-quality cells/
nuclei noted above, and then centered and scaled values before inputting them into principal
component analysis (PCA), implemented using 'RunPCA' in Seurat which runs the *irlba*
function. For the snRNA-seq data, which included mixed sexes, we removed Y-chromosome
and X-inactivation genes (*Xist, Tsix*) from the variable genes prior to running PCA. The cell
embeddings were either the singular vectors themselves or the singular vectors multiplied
with the singular values depending on the cell type. After PCA, significant principal
components were identified using the elbow-method, when looking at the distribution of
singular values. Scores from only those significant principal components were used as the
input to further analysis. For visualization purposes, the dimensionality of the datasets was
further reduced to 2D embeddings using t-SNE (for scRNA-seq) (Van Der Maaten and
Hinton, 2008) or UMAP (Becht et al., 2019) (for snRNA-seq) on the significant PCs using,
respectively, the RunTSNE() or RunUMAP() functions of the *Seurat* package in R.

Clustering and removing doublets in scRNA-seq data—To cluster single cells by
their expression, we used an unsupervised clustering approach, based on the Infomap graph-
clustering algorithm (Girvan and Newman, 2002). In brief, we constructed a *k*-nearest-
neighbor graph on the data using, for each pair of cells, the Euclidean distance between the
scores of significant principal components to identify *k* nearest neighbors. The parameter *k*
was chosen to be consistent with the size of the dataset. Specifically, *k* was set to 40 for
neuronal/glia-like cells and to 20 for immune cells, for which subclusters of macrophages
were *post-hoc* merged together based on expression of canonical markers. The nearest-
neighbor graph was computed using the function *nng* from the R package *cccd*. The *k*-
nearest-neighbor graph was then used as the input to Infomap (Girvan and Newman, 2002),
implemented using the *infomap.community* function from the *igraph* R package. For major
cell types (Figure 1C), clusters were *post-hoc* merged to six major cell populations using
canonical markers for all cell types detected.

Doublets were clearly identifiable as forming their own clusters with dual expression of
marker genes of distinct subsets (*e.g.,* epithelial genes and endothelial genes) and were
removed from further analysis and any visualizations.

Removing doublets in snRNA-seq data—Nucleus doublets were identified using the
R package DoubletFinder (version DoubletFinder_2.0.2, (McGinnis et al., 2019). Briefly,
artificial doublets are generated from the data, and for each real data point the fraction of
artificial doublets of the nearest neighbors in a latent space is computed. If this fraction is
above a certain cutoff, the data point is considered to be a doublet. Doublets were calculated
for each sample separately after initial data filtering by genes detected and mitochondrial
gene expression as per instructions. For each sample, an optimal pK (defines the PC
neighborhood size) was chosen by computing a parameter sweep (paramSweep_v3 function)
and a pK was chosen that maximized the BCmvn (mean-variance-normalized bimodality
coefficient). Doublets were then calculated using the function doubletFinder_v3() with
parameters; PCs=1:30, pN=0.25, nEXP=15% of cells in sample and removed from
downstream analysis.

Scoring cells using signature gene sets—In order to score cells using a gene sets, such as cell cycle (Figure 2A) or arterial / venous gene expression (Figure S5A), we calculate the following gene signature score: Mean program expression was calculated by averaging over the genes in each program of the centered and scaled gene expression table and transforming to a z-score over 1,000 randomly selected gene sets with matched mean-variance patterns. First, genes were grouped into 10 bins based on their mean expression, and into 10 (separate) bins based on their variance of expression across all cells. Given a list of genes (e.g. genes in a program), a cell-specific signature score was computed for each cell as follows: First, 1,000 random gene lists were generated, where each instance of a random gene-list was generated by sampling (with replacement) for each gene in the gene-list a gene from the equivalent mean and variance bin it was placed in. Then, the sum of centered and scaled gene expression in the given cell was computed for all 1000 random gene-lists generated and the z-score of the original gene-list for the generated 1,000 sample distribution is returned, as in (Singer et al., 2016). For cycling cells, cells with a z-score above 2 were classified as cycling cells.

Topic modeling—We performed topic modeling using Latent Dirichlet Allocation (LDA). LDA was computed on epithelial, mesenchymal and endothelial cells separately in the embryo, and on epithelial cells in adult. Specifically, we used the FitGoM() function from the *CountClust* R package (Dey et al., 2017) to fit LDA topic models to the UMI counts (Bielecki et al., 2021). To improve topic signals, genes expressed in more than 98% of cells or less than 2% of cells were removed from the count matrix prior to fitting the topic models (analogous to the removal of highly abundant words or extremely rare words in document analysis), except for endothelial cells. The number of topics to fit (K) and the tolerance value are required to run FitGoM() function. Thus, for each cell type and developmental status, we fit a range of K and tolerance values and picked values that gave us robust topics and where we mostly saturated the number of informative topics found. For the embryo data, this was achieved with a tolerance of 0.1, and a K of 16 for endothelial cells, K of 26 for epithelial and mesenchymal cells, and K of 14 and tolerance of 0.01 for adult epithelial nuclei. The top genes to highlight for each topic were selected using the ExtractTopFeatures() function. Topics were annotated post-hoc. Notably, in the analysis of epithelial cells, one topic was enriched for immediate early genes (Topic 19, Figure S3B,C) and may reflect a response to tissue dissociation (van den Brink et al., 2017) because it was reduced in single nucleus profiles (Lacar et al., 2016) (Figure S3D).

Defining cell-type or cluster signatures—Differential expression between cell types in scRNA-Seq of embryo (Figure 1) and between clusters of immune cells and neuro-/glia-like cells in scRNA-Seq was performed using MAST (Finak et al., 2015), which fits a hurdle model to the expression of each gene, consisting of logistic regression for the zero component (*i.e.* whether the gene is expressed) and linear regression for the continuous component (*i.e.* the expression level). The regression model includes terms to capture the effects of the cell subset or cluster, while controlling for cell complexity (*i.e.* the total number of UMIs (nUMI)). Specifically, we used the regression formula, $Yi \sim X + N$, where Yi is the standardized $\log_2$(TP10K+1) expression vector for gene i across all cells, X is a factor variable reflecting cell subset or cluster membership, N is the scaled nUMI in each

cell. In all cases, the discrete and continuous coefficients of the model were retrieved and p-values were calculated using the likelihood ratio test in MAST. Q-values were estimated using the Benjamini-Hochberg correction. In order to identify cell-type specific or cluster specific markers, an FDR cutoff for the hurdle model was chosen using the elbow-method and a small mastfc cutoff to exclude genes with very small effect sizes. If a gene passed the FDR and the mastfc cutoff in only one cluster / cell type, it was considered to be specific.

Cell type classification of scRNA-seq dataset using snRNA-seq dataset of embryo—To compare embryo scRNA-seq dataset to embryo snRNA-seq, a random forest classifier was used from the R package 'randomForest'. First, common variable genes were computed between the two datasets by taking the intersection of the variable genes in each dataset. Then, the classifier was trained on the scaled expression matrix of the common variable genes in the embryo snRNA-seq dataset. The out-of-bag error was 1.7%. The classifier then ran on the scaled expression matrix of the common variable genes in the embryo scRNA-seq dataset. We then compared the predicted cell type assignment of the random forest classifier to our own cell type assignment shown in Figure 1C.

Diffusion map—For diffusion analysis of embryo epithelial and neuronal cells, we selected cells from only 3V ChP, where most neuronal and glial cells were sampled from, and only from replicate 3, because of strong batch effects between replicates. Furthermore, the epithelial cell clusters scoring highly for IEG genes (Figure S2D) and oligodendrocyte precursor cells were also excluded from this analysis. Of the remaining cells, variable genes were computed as described above. Diffusion components were calculated on a gene expression matrix limited to variable genes within the selected cells (not correcting for batch). Diffusion components were calculated using the DiffusionMap function from the *destiny* package in R (Angerer et al., 2016) with a k of 30 and a local sigma.

For macrophages, cells of replicate 3 were excluded for this analysis because they had very high expression of mitochondrial genes. Diffusion components were calculated as above on a gene expression matrix limited to variable genes within the macrophages (not correcting for batch) with a k of 20 and a local sigma.

RNA Velocity analysis of epithelial-neuronal trajectory—To study the inferred trajectory of epithelial-neuronal differentiation (Figure 2), RNA velocity analysis was performed, which compares reads mapped to exonic versus intronic regions to assess the future transcriptional state of the cell. We ran the function gene.relative.velocity.estimates() of the velocyto package in R on the cells used in the trajectory analysis in Figure 2 and variable genes as described above. We used the 1-correlation of the first 16 diffusion components as a cell distance measure, and deltaT=1, kCells=25, fit.quantile=0.02. The RNA velocity vectors were visualized on the trajectory embedding from the diffusion analysis.

Pseudo-bulk analysis of epithelial and fibroblast cells to test for significantly differentially expressed genes between age and ventricle—To conservatively identify high confidence genes that vary with age and/or ventricle, we performed pseudo-bulk analysis for epithelial cells and fibroblast (excluding meningeal cells, pericytes and

vSMCs). To that end, all UMIs were summed within each sample of a specific age and ventricle. Because the samples consisted of pooled mice from both sexes, the fraction of male genes expression in each sample was normalized by the sum of all UMIs from y-chromosome genes (by introducing a covariate was termed tUMI.ygens). Then, we performed differential expression analysis using DESeq2 package in R, where the data was the total UMIs as described above per sample. The expression modeling was '~ tUMI.ygenes + Stage + Ventricle + Stage:Ventricle, where Stage denotes pre- or post-natal (including both adult and aged samples). A separate DESeq2 analysis was performed for testing for differentially expressed genes between Adult and Aged, with a likelihood-ratio test against a reduced model of '~tUMI.ygenes + Ventricle' to identify age-effects (adjusted p-value cutoff used by elbow method was 10^{-5} for epithelial cells and fibroblast) or '~tUMI.ygenes + Stage' to identify regionalized genes (adjusted p-value cutoff used by elbow method; Epithelial = 10^{-15}, Fibroblast = 10^{-3}) and required the absolute log2FoldChange to be >1 to filter out genes with significant but small effect size. For visualization of the significantly differentially expressed genes, normalized values of these pseudo-bulk samples were scaled, and capped at an absolute z-score of 2.5.

Cell-cell interactions—To quantify cell-cell interactions between major cell types across age, we used CellPhoneDB (Efremova et al., 2020) on all cells of embryo, adult and aged ChP separately. In short, this method computes the average expression of a ligand-receptor pair for each pair of cell type provided as a meta file. It then computes an empirical p-value to the specificity of this interaction by permuting cell types identity 1,000 times and comparing the real average expression against this null distribution. As CellPhoneDB is developed for human ligand-cognate receptor pairs, gene names were converted to their human homolog, removing genes for which no one-to-one human homolog could be associated.

Significant cell-type pair ligand-receptor interactions were used as edges for a directed cell-cell interaction graph. For pairs lacking clear ligand and receptor notations, we could not infer the directionality of the interaction by the annotation, and thus the directionality of the edge was determined by the CellPhoneDB annotation (given that the statistical significance assigned to each pair of cells has a clear direction). Next, to calculate the statistical significance of the strength of estimated interaction between pairs of cell types (in a specific age and ventricle), we performed two types of permutation tests – in each test we perform 10,000 permutations and calculate an empirical p-value for the number of interactions found for a pair of cell types. The tests were: (1) maintaining the total number of edges and randomizing the ligand- and receptor-cell type assignments; and (2) maintaining the total number of edges per each cell type (the degree of the nodes) and permutating the cell type source and destination of the edge (the ligand-receptor pair).

Differential interaction graphs, over different ages or ventricles were constructed based on the unique edges of each dataset. We define a differential edge, as a ligand-receptor pair that were found to be both statistically significant expressed in the respective pair of cell types under one condition (age and ventricle) but not in another condition compared to it. A similar permutation strategy was used to compute an empirical p-value for the differential interaction graphs.

To visualize interaction graphs, we used Sankey plots, using the Sankey Network function of the networkD3 package, showing the number of edges between ligand expressing- and receptor expressing cell types. We combined two Sankey plots to show the differential graphs between two conditions.

Supplementary Material

Refer to Web version on PubMed Central for supplementary material.

ACKNOWLEDGEMENTS

REFERENCES

Angerer P, Haghverdi L, Büttner M, Theis FJ, Marr C, and Buettner F (2016). Destiny: Diffusion maps for large-scale single-cell data in R. Bioinformatics 32, 1241–1243. [PubMed: 26668002]

Awatramani R, Soriano P, Rodriguez C, Mai JJ, and Dymecki SM (2003). Cryptic boundaries in roof plate and choroid plexus identified by intersectional gene activation. Nat. Genet 35, 70–75.

Awatramanil R, Soriano P, Rodriguez C, Mai JJ, and Dymecki SM (2003). Cryptic boundaries in roof plate and choroid plexus identified by intersectional gene activation. Nat. Genet 35, 70–75.

Baruch K, Deczkowska A, David E, Castellano JM, Miller O, Kertser A, Berkutzki T, Barnett-Itzhaki Z, Bezalel D, Wyss-Coray T, et al. (2014). Aging-induced type I interferon response at the choroid plexus negatively affects brain function. Science (80-.). 346, 89–93.

Becht E, McInnes L, Healy J, Dutertre CA, Kwok IWH, Ng LG, Ginhoux F, and Newell EW (2019). Dimensionality reduction for visualizing single-cell data using UMAP. Nat. Biotechnol 37, 38–47.

Bell SM, Schreiner CM, Wert SE, Mucenski ML, Scott WJ, and Whitsett JA (2008). R-spondin 2 is required for normal laryngeal-tracheal, lung and limb morphogenesis. Development 135, 1049–1058. [PubMed: 18256198]

Ben-Zvi A, Lacoste B, Kur E, Andreone BJ, Mayshar Y, Yan H, and Gu C (2014). Mfsd2a is critical for the formation and function of the blood–brain barrier. Nature 509, 507–511. [PubMed: 24828040]

Bielecki P, Riesenfeld SJ, Hutter JC, Torlai Triglia E, Kowalczyk MS, Ricardo-Gonzalez RR, Lian M, Amezcua Vesely MC, Kroehling L, Xu H, et al. (2021). Skin-resident innate lymphoid cells converge on a pathogenic effector state. Nature.

Blei D, Ng A, and Jordan M (2003). Latent Dirichlet Allocation.

van den Brink SC, Sage F, Vértesy Á, Spanjaard B, Peterson-Maduro J, Baron CS, Robin C, and van Oudenaarden A (2017). Single-cell sequencing reveals dissociation-induced gene expression in tissue subpopulations. Nat. Methods 14, 935–936. [PubMed: 28960196]

Brooks ER, and Wallingford JB (2014). Multiciliated Cells. Curr. Biol 24, R973–R982. [PubMed: 25291643]

Cantuti-Castelvetri L, Ojha R, Pedro LD, Djannatian M, Franz J, Kuivanen S, van der Meer F, Kallio K, Kaya T, Anastasina M, et al. (2020). Neuropilin-1 facilitates SARS-CoV-2 cell entry and infectivity. Science (80-.). 370, eabd2985.

Chang JT, Lehtinen MK, and Sive H (2016). Zebrafish cerebrospinal fluid mediates cell survival through a retinoid signaling pathway. Dev. Neurobiol 76, 75–92. [PubMed: 25980532]

Chuang P-T, and McMahon AP (1999). Vertebrate Hedgehog signalling modulated by induction of a Hedgehog-binding protein. Nature 397, 617–621. [PubMed: 10050855]

Cui J, Shipley FB, Shannon ML, Alturkistani O, Dani N, Webb MD, Sugden AU, Andermann ML, and Lehtinen MK (2020). Inflammation of the Embryonic Choroid Plexus Barrier following Maternal Immune Activation. Dev. Cell 55(5), 617–628. [PubMed: 33038331]

Damkier HH, Brown PD, and Praetorius J (2013). Cerebrospinal Fluid Secretion by the Choroid Plexus. Physiol. Rev 93, 1847–1892. [PubMed: 24137023]

DeSisto J, O'Rourke R, Jones HE, Pawlikowski B, Malek AD, Bonney S, Guimiot F, Jones KL, and Siegenthaler JA (2020). Single-Cell Transcriptomic Analyses of the Developing Meninges Reveal Meningeal Fibroblast Diversity and Function. Dev. Cell 54, 43–59.e4. [PubMed: 32634398]

Dey KK, Hsiao CJ, and Stephens M (2017). Visualizing the structure of RNA-seq expression data using grade of membership models. PLOS Genet. 13, e1006599. [PubMed: 28333934]

Dulken BW, Leeman DS, Boutet SC, Hebestreit K, and Brunet A (2017). Single-Cell Transcriptomic Analysis Defines Heterogeneity and Transcriptional Dynamics in the Adult Neural Stem Cell Lineage. Cell Rep. 18, 777–790. [PubMed: 28099854]

Eden E, Lipson D, Yogev S, and Yakhini Z (2007). Discovering motifs in ranked lists of DNA sequences. PLoS Comput. Biol 3, 0508–0522.

Eden E, Navon R, Steinfeld I, Lipson D, and Yakhini Z (2009). GOrilla: A tool for discovery and visualization of enriched GO terms in ranked gene lists. BMC Bioinformatics 10:48. [PubMed: 19192299]

Efremova M, Vento-Tormo M, Teichmann SA, and Vento-Tormo R (2020). CellPhoneDB: inferring cell–cell communication from combined expression of multi-subunit ligand–receptor complexes. Nat. Protoc 15, 1484–1506. [PubMed: 32103204]

Ellul MA, Benjamin L, Singh B, Lant S, Michael BD, Easton A, Kneen R, Defres S, Sejvar J, and Solomon T (2020). Neurological associations of COVID-19. Lancet Neurol. 19(9):767–783. [PubMed: 32622375]

Fame RM, and Lehtinen MK (2020). Emergence and Developmental Roles of the Cerebrospinal Fluid System. Dev. Cell 52, 261–275. [PubMed: 32049038]

Finak G, McDavid A, Yajima M, Deng J, Gersuk V, Shalek AK, Slichter CK, Miller HW, McElrath MJ, Prlic M, et al. (2015). MAST: a flexible statistical framework for assessing transcriptional changes and characterizing heterogeneity in single-cell RNA sequencing data. Genome Biol. 16, 278. [PubMed: 26653891]

Fleming SJ, Marioni JC, and Babadi M (2019). CellBender remove-background: A deep generative model for unsupervised removal of background noise from scRNA-seq datasets. BioRxiv 791699.

Gaublomme JT, Li B, McCabe C, Knecht A, Yang Y, Drokhlyansky E, Van Wittenberghe N, Waldman J, Dionne D, Nguyen L, et al. (2019). Nuclei multiplexing with barcoded antibodies for single-nucleus genomics. Nat. Commun 10(1), 2907. [PubMed: 31266958]

Ghersi-Egea J-F, Strazielle N, Catala M, Silva-Vargas V, Doetsch F, and Engelhardt B (2018). Molecular anatomy and functions of the choroidal blood-cerebrospinal fluid barrier in health and disease. Acta Neuropathol. 135, 337–361. [PubMed: 29368213]

Girvan M, and Newman MEJ (2002). Community structure in social and biological networks. Proc. Natl. Acad. Sci. U. S. A 99, 7821–7826. [PubMed: 12060727]

Habib N, Avraham-Davidi I, Basu A, Burks T, Shekhar K, Hofree M, Choudhury SR, Aguet F, Gelfand E, Ardlie K, et al. (2017). Massively parallel single-nucleus RNA-seq with DroNc-seq. Nat. Methods 14, 955–958. [PubMed: 28846088]

Hagan N, and Zervas M (2012). Wnt1 expression temporally allocates upper rhombic lip progenitors and defines their terminal cell fate in the cerebellum. Mol. Cell. Neurosci 49, 217–229. [PubMed: 22173107]

Haghverdi L, Büttner M, Wolf FA, Buettner F, and Theis FJ (2016). Diffusion pseudotime robustly reconstructs lineage branching. Nat. Methods 13, 845–848. [PubMed: 27571553]

Haldar M, Kohyama M, So AY-L, KC W, Wu X, Briseño CG, Satpathy AT, Kretzer NM, Arase H, Rajasekaran NS, et al. (2014). Heme-Mediated SPI-C Induction Promotes Monocyte Differentiation into Iron-Recycling Macrophages. Cell 156, 1223–1234. [PubMed: 24630724]

Hammond TR, Dufort C, Dissing-Olesen L, Giera S, Young A, Wysoker A, Walker AJ, Gergits F, Segel M, Nemesh J, et al. (2019). Single-Cell RNA Sequencing of Microglia throughout the Mouse Lifespan and in the Injured Brain Reveals Complex Cell-State Changes. Immunity 50, 253–271.e6. [PubMed: 30471926]

Herrnberger L, Seitz R, Kuespert S, Bösl MR, Fuchshofer R, and Tamm ER (2012). Lack of endothelial diaphragms in fenestrae and caveolae of mutant Plvap-deficient mice. Histochem. Cell Biol 138, 709–724. [PubMed: 22782339]

Van Hove H, Martens L, Scheyltjens I, De Vlaminck K, Rita Pombo Antunes A, De Prijck S, Vandamme N, De Schepper S, Van Isterdael G, Scott CL, et al. (2019). A single-cell atlas of mouse brain macrophages reveals unique transcriptional identities shaped by ontogeny and tissue environment. Nat. Neurosci 22(6):1021–1035. [PubMed: 31061494]

Huang X, Ketova T, Fleming JT, Wang H, Dey SK, Litingtung Y, and Chiang C (2009). Sonic hedgehog signaling regulates a novel epithelial progenitor domain of the hindbrain choroid plexus. Development 136, 2535–2543. [PubMed: 19570847]

Hudson AJ (1960). The development of the vascular pattern of the choroid plexus of the lateral ventricles. J. Comp. Neurol 115, 171–186. [PubMed: 13716507]

Hunter NL, and Dymecki SM (2007). Molecularly and temporally separable lineages form the hindbrain roof plate and contribute differentially to the choroid plexus. Development 134, 3449–3460. [PubMed: 17728348]

Jordão MJC, Sankowski R, Brendecke SM, Sagar, Locatelli G, Tai Y-H, Tay TL, Schramm E, Armbruster S, Hagemeyer N, et al. (2019a). Single-cell profiling identifies myeloid cell subsets with distinct fates during neuroinflammation. Science 363, eaat7554.

Kaiser K, Gyllborg D, Procházka J, Salašová A, Kompaníková P, Molina FL, Laguna-Goya R, Radaszkiewicz T, Harnoš J, Procházková M, et al. (2019). WNT5A is transported via lipoprotein particles in the cerebrospinal fluid to regulate hindbrain morphogenesis. Nat. Commun 10(1):1498.

Kania A, and Klein R (2016). Mechanisms of ephrin-Eph signalling in development, physiology and disease. Nat. Rev. Mol. Cell Biol 17, 240–256. [PubMed: 26790531]

Karimy JK, Zhang J, Kurland DB, Theriault BC, Duran D, Stokum JA, Furey CG, Zhou X, Mansuri MS, Montejo J, et al. (2017). Inflammation-dependent cerebrospinal fluid hypersecretion by the choroid plexus epithelium in posthemorrhagic hydrocephalus. Nat. Med 23, 997–1003. [PubMed: 28692063]

Keep RF, and Jones HC (1990). A morphometric study on the development of the lateral ventricle choroid plexus, choroid plexus capillaries and ventricular ependyma in the rat. Dev. Brain Res 56, 47–53. [PubMed: 2279331]

Kinzel B, Pikiolek M, Orsini V, Sprunger J, Isken A, Zietzling S, Desplanches M, Dubost V, Breustedt D, Valdez R, et al. (2014). Functional roles of Lgr4 and Lgr5 in embryonic gut, kidney and skin development in mice. Dev. Biol 390, 181–190. [PubMed: 24680895]

Kohyama M, Ise W, Edelson BT, Wilker PR, Hildner K, Mejia C, Frazier WA, Murphy TL, and Murphy KM (2009). Role for Spi-C in the development of red pulp macrophages and splenic iron homeostasis. Nature 457, 318–321. [PubMed: 19037245]

Krausgruber T, Fortelny N, Fife-Gernedl V, Senekowitsch M, Schuster LC, Lercher A, Nemc A, Schmidl C, Rendeiro AF, Bergthaler A, et al. (2020). Structural cells are key regulators of organ-specific immune responses. Nature 583, 296–302. [PubMed: 32612232]

Kriegstein A, and Alvarez-Buylla A (2009). The glial nature of embryonic and adult neural stem cells. Annu. Rev. Neurosci 32, 149–184. [PubMed: 19555289]

Kuro-o M, Matsumura Y, Aizawa H, Kawaguchi H, Suga T, Utsugi T, Ohyama Y, Kurabayashi M, Kaname T, Kume E, et al. (1997). Mutation of the mouse klotho gene leads to a syndrome resembling ageing. Nature 390, 45–51. [PubMed: 9363890]

Lacar B, Linker SB, Jaeger BN, Krishnaswami S, Barron J, Kelder M, Parylak S, Paquola A, Venepally P, Novotny M, et al. (2016). Nuclear RNA-seq of single neurons reveals molecular signatures of activation. Nat. Commun 7:11022. [PubMed: 27090946]

Leek JT, Johnson WE, Parker HS, Jaffe AE, and Storey JD (2012). The sva package for removing batch effects and other unwanted variation in high-throughput experiments. Bioinformatics 28, 882–883. [PubMed: 22257669]

Lehtinen MK, Zappaterra MW, Chen X, Yang YJ, Hill AD, Lun M, Maynard T, Gonzalez D, Kim S, Ye P, et al. (2011). The Cerebrospinal Fluid Provides a Proliferative Niche for Neural Progenitor Cells. Neuron 69, 893–905. [PubMed: 21382550]

Lein ES, Hawrylycz MJ, Ao N, Ayres M, Bensinger A, Bernard A, Boe AF, Boguski MS, Brockway KS, Byrnes EJ, et al. (2007). Genome-wide atlas of gene expression in the adult mouse brain. Nature 445, 168–176. [PubMed: 17151600]

Lewis AE, Vasudevan HN, O'Neill AK, Soriano P, and Bush JO (2013). The widely used Wnt1-Cre transgene causes developmental phenotypes by ectopic activation of Wnt signaling. Dev. Biol 379, 229–234. [PubMed: 23648512]

Li Q, Cheng Z, Zhou L, Darmanis S, Neff NF, Okamoto J, Gulati G, Bennett ML, Sun LO, Clarke LE, et al. (2019). Developmental Heterogeneity of Microglia and Brain Myeloid Cells Revealed by Deep Single-Cell RNA Sequencing. Neuron 101, 207–223.e10. [PubMed: 30606613]

Liddelow SA, Dziegielewska KM, VandeBerg JL, and Saunders NR (2010). Development of the lateral ventricular choroid plexus in a marsupial, Monodelphis domestica. Cerebrospinal Fluid Res. 7, 16. [PubMed: 20920364]

Lim HY, Lim SY, Tan CK, Thiam CH, Goh CC, Carbajo D, Chew SHS, See P, Chakarov S, Wang XN, et al. (2018). Hyaluronan Receptor LYVE-1-Expressing Macrophages Maintain Arterial Tone through Hyaluronan-Mediated Regulation of Smooth Muscle Cell Collagen. Immunity 49, 326–341.e7. [PubMed: 30054204]

Lindvall M, Edvinsson L, and Owman C (1978). Sympathetic nervous control of cerebrospinal fluid production from the choroid plexus. Science 201, 176–178. [PubMed: 663649]

Livet J, Weissman TA, Kang H, Draft RW, Lu J, Bennis RA, Sanes JR, and Lichtman JW (2007). Transgenic strategies for combinatorial expression of fluorescent proteins in the nervous system. Nature 450, 56–62. [PubMed: 17972876]

Louvi A, and Wassef M (2000). Ectopic Engrailed 1 expression in the dorsal midline causes cell death, abnormal differentiation of circumventricular organs and errors in axonal pathfinding. Development 127, 4061–4071. [PubMed: 10952903]

Lun MP, Monuki ES, and Lehtinen MK (2015a). Development and functions of the choroid plexus–cerebrospinal fluid system. Nat. Rev. Neurosci. 16, 445–457. [PubMed: 26174708]

Lun MP, Johnson MB, Broadbelt KG, Watanabe M, Kang YJ, Chau KF, Springel MW, Malesz A, Sousa AM, Pletikos M, et al. (2015b). Spatially heterogeneous choroid plexus transcriptomes encode positional identity and contribute to regional CSF production. J Neurosci 35, 4903–4916. [PubMed: 25810521]

Van Der Maaten L, and Hinton G (2008). Visualizing Data using t-SNE.

Mancini M, Greco A, Tedeschi E, Palma G, Ragucci M, Bruzzone MG, Coda ARD, Torino E, Scotti A, Zucca I, et al. (2015). Head and neck veins of the mouse. A magnetic resonance, micro computed tomography and high frequency color Doppler ultrasound study. PLoS One 10(6):e0129912.

La Manno G, Soldatov R, Zeisel A, Braun E, Hochgerner H, Petukhov V, Lidschreiber K, Kastriti ME, Lönnerberg P, Furlan A, et al. (2018). RNA velocity of single cells. Nature 560, 494–498. [PubMed: 30089906]

Martik ML, and Bronner ME (2017). Regulatory Logic Underlying Diversification of the Neural Crest. Trends Genet. 33, 715–727. [PubMed: 28851604]

Mathew RS, Mullan H, Blusztajn JK, and Lehtinen MK (2016). Comment on "Multiple repressive mechanisms in the hippocampus during memory formation". Science 353, 453.

Mazucanti CH, Liu QR, Lang D, Huang N, O'Connell JF, Camandola S, and Egan JM (2019). Release of insulin produced by the choroids plexis is regulated by serotonergic signaling. JCI Insight 4(23):e131682.

McGinnis CS, Murrow LM, and Gartner ZJ (2019). DoubletFinder: Doublet Detection in Single-Cell RNA Sequencing Data Using Artificial Nearest Neighbors. Cell Syst. 8, 329–337.e4. [PubMed: 30954475]

Mizrak D, Levitin HM, Delgado AC, Crotet V, Yuan J, Chaker Z, Silva-Vargas V, Sims PA, and Doetsch F (2019). Single-Cell Analysis of Regional Differences in Adult V-SVZ Neural Stem Cell Lineages. Cell Rep. 26, 394–406.e5. [PubMed: 30625322]

Montoro DT, Haber AL, Biton M, Vinarsky V, Lin B, Birket SE, Yuan F, Chen S, Leung HM, Villoria J, et al. (2018). A revised airway epithelial hierarchy includes CFTR-expressing ionocytes. Nature 560, 319–324. [PubMed: 30069044]

Muus C, Luecken M, Eraslan G, Waghray A, Heimberg G, Sikkema L, Kobayashi Y, Vaishnav ED, Subramanian A, Smilie C, et al. (2020). Integrated analyses of single-cell atlases reveal age, gender, and smoking status associations with cell type-specific expression of mediators of SARS-CoV-2 viral entry and highlights inflammatory programs in putative target cells. BioRxiv 2020.04.19.049254.

Myung J, Schmal C, Hong S, Tsukizawa Y, Rose P, Zhang Y, Holtzman MJ, De Schutter E, Herzel H, Bordyugov G, et al. (2018). The choroid plexus is an important circadian clock component. Nat. Commun 9, 1062. [PubMed: 29540683]

Paré A, Mailhot B, Lévesque SA, Juzwik C, Doss PMIA, Lécuyer MA, Prat A, Rangachari M, Fournier A, and Lacroix S (2018). IL-1β enables CNS access to CCR2hi monocytes and the generation of pathogenic cells through GM-CSF released by CNS endothelial cells. Proc. Natl. Acad. Sci. U. S. A. 115, E1194–E1203. [PubMed: 29358392]

Pellegrini L, Albecka A, Mallery DL, Kellner MJ, Paul D, Carter AP, James LC, and Lancaster MA (2020a). SARS-CoV-2 Infects the Brain Choroid Plexus and Disrupts the Blood-CSF Barrier in Human Brain Organoids. Cell Stem Cell. 27(6):951–961. [PubMed: 33113348]

Pellegrini L, Bonfio C, Chadwick J, Begum F, Skehel M, and Lancaster MA (2020b). Human CNS barrier-forming organoids with cerebrospinal fluid production. Science. 369(6500):eaaz5626. [PubMed: 32527923]

Pritchard JK, Stephens M, and Donnelly P (2000). Inference of Population Structure Using Multilocus Genotype Data. Genetics 155(2):945–59. [PubMed: 10835412]

Reboldi A, Coisne C, Baumjohann D, Benvenuto F, Bottinelli D, Lira S, Uccelli A, Lanzavecchia A, Engelhardt B, and Sallusto F (2009). C-C chemokine receptor 6–regulated entry of TH-17 cells into the CNS through the choroid plexus is required for the initiation of EAE. Nat. Immunol 10, 514–523. [PubMed: 19305396]

Saunders A, Macosko EZ, Wysoker A, Goldman M, Krienen FM, de Rivera H, Bien E, Baum M, Bortolin L, Wang S, et al. (2018a). Molecular Diversity and Specializations among the Cells of the Adult Mouse Brain. Cell 174, 1015–1030.e16. [PubMed: 30096299]

Saunders NR, Dziegielewska KM, Møllgård K, and Habgood MD (2018b). Physiology and molecular biology of barrier mechanisms in the fetal and neonatal brain. J. Physiol 596, 5723–5756. [PubMed: 29774535]

Schiebinger G, Shu J, Tabaka M, Cleary B, Subramanian V, Solomon A, Gould J, Liu S, Lin S, Berube P, et al. (2019). Optimal-Transport Analysis of Single-Cell Gene Expression Identifies Developmental Trajectories in Reprogramming. Cell 176, 928–943.e22. [PubMed: 30712874]

Schwartz M, and Baruch K (2014). The resolution of neuroinflammation in neurodegeneration: Leukocyte recruitment via the choroid plexus. EMBO J. 33, 7–22. [PubMed: 24357543]

Shah PT, Stratton JA, Stykel MG, Abbasi S, Sharma S, Mayr KA, Koblinger K, Whelan PJ, and Biernaskie J (2018). Single-Cell Transcriptomics and Fate Mapping of Ependymal Cells Reveals an Absence of Neural Stem Cell Function. Cell 173, 1045–1057.e9. [PubMed: 29727663]

Shannon ML, Fame RM, Chau KF, Dani N, Calicchio ML, Géléoc GS, Lidov HGW, Alexandrescu S, and Lehtinen MK (2018). Mice Expressing Myc in Neural Precursors Develop Choroid Plexus and Ciliary Body Tumors. Am. J. Pathol 188, 1334–1344. [PubMed: 29545198]

Shechter R, Miller O, Yovel G, Rosenzweig N, London A, Ruckh J, Kim K-W, Klein E, Kalchenko V, Bendel P, et al. (2013). Recruitment of beneficial M2 macrophages to injured spinal cord is orchestrated by remote brain choroid plexus. Immunity 38, 555–569. [PubMed: 23477737]

Shipley FB, Dani N, Xu H, Deister C, Cui J, Head JP, Sadegh C, Fame RM, Shannon ML, Flores VI, et al. (2020). Tracking Calcium Dynamics and Immune Surveillance at the Choroid Plexus Blood-Cerebrospinal Fluid Interface. Neuron. 108(4):623–639. [PubMed: 32961128]

Shuangshoti S, and Netsky MG (1966). Histogenesis of choroid plexus in man. Am. J. Anat 118, 283–315. [PubMed: 5915034]

Silva-Vargas V, Maldonado-Soto ARR, Mizrak D, Codega P, and Doetsch F (2016). Age-Dependent Niche Signals from the Choroid Plexus Regulate Adult Neural Stem Cells. Cell Stem Cell 19, 643–652. [PubMed: 27452173]

Singer M, Wang C, Cong L, Marjanovic ND, Kowalczyk MS, Zhang H, Nyman J, Sakuishi K, Kurtulus S, Gennert D, et al. (2016). A Distinct Gene Module for Dysfunction Uncoupled from Activation in Tumor-Infiltrating T Cells. Cell 166, 1500–1511.e9. [PubMed: 27610572]

Snippert HJ, van der Flier LG, Sato T, van Es JH, van den Born M, Kroon-Veenboer C, Barker N, Klein AM, van Rheenen J, Simons BD, et al. (2010). Intestinal crypt homeostasis results from neutral competition between symmetrically dividing Lgr5 stem cells. Cell 143, 134–144. [PubMed: 20887898]

Tong Y, Merino D, Nimmervoll B, Gupta K, Wang YD, Finkelstein D, Dalton J, Ellison DW, Ma X, Zhang J, et al. (2015). Cross-Species Genomics Identifies TAF12, NFYC, and RAD54L as Choroid Plexus Carcinoma Oncogenes. Cancer Cell 27, 712–727. [PubMed: 25965574]

Vanlandewijck M, He L, Mäe MA, Andrae J, Ando K, Del Gaudio F, Nahar K, Lebouvier T, Laviña B, Gouveia L, et al. (2018). A molecular atlas of cell types and zonation in the brain vasculature. Nature 554, 475–480. [PubMed: 29443965]

Visel A, Thaller C, and Eichele G (2004). GenePaint.org: an atlas of gene expression patterns in the mouse embryo. Nucleic Acids Res. 32, D552–6. [PubMed: 14681479]

Wang F, Flanagan J, Su N, Wang L-C, Bui S, Nielson A, Wu X, Vo H-T, Ma X-J, and Luo Y (2012). RNAscope: a novel in situ RNA analysis platform for formalin-fixed, paraffin-embedded tissues. J. Mol. Diagn 14, 22–29. [PubMed: 22166544]

Wilting J, and Christ B (1989). An experimental and ultrastructural study on the development of the avian choroid plexus. Cell Tissue Res. 255, 487–494. [PubMed: 2706656]

Wingate RJT (2001). The rhombic lip and early cerebellar development. Curr. Opin. Neurobiol 11, 82–88. [PubMed: 11179876]

Wu Y, Xu X, Chen Z, Duan J, Hashimoto K, Yang L, Liu C, and Yang C (2020). Nervous system involvement after infection with COVID-19 and other coronaviruses. Brain. Behav. Immun 87, 18–22. [PubMed: 32240762]

Xu H, Fame RM, Sadegh C, Sutin J, Naranjo C, Della Syau, Cui J, Shipley FB, Vernon A, Gao F, et al. (2021). Choroid plexus NKCC1 mediates cerebrospinal fluid clearance during mouse early postnatal development. Nat. Commun 12(1):447. [PubMed: 33469018]

Yang AC, Kern F, Losada PM, Maat CA, Schmartz G, Fehlmann T, Schaum N, Lee DP, Calcuttawala K, Vest RT, et al. (2020). Broad transcriptional dysregulation of brain and choroid plexus cell types with COVID-19. BioRxiv 2020.10.22.349415.

Zhu L, Stein LR, Kim D, Ho K, Yu G-Q, Zhan L, Larsson TE, and Mucke L (2018). Klotho controls the brain-immune system interface in the choroid plexus. Proc. Natl. Acad. Sci. U. S. A 115, E11388–E11396. [PubMed: 30413620]
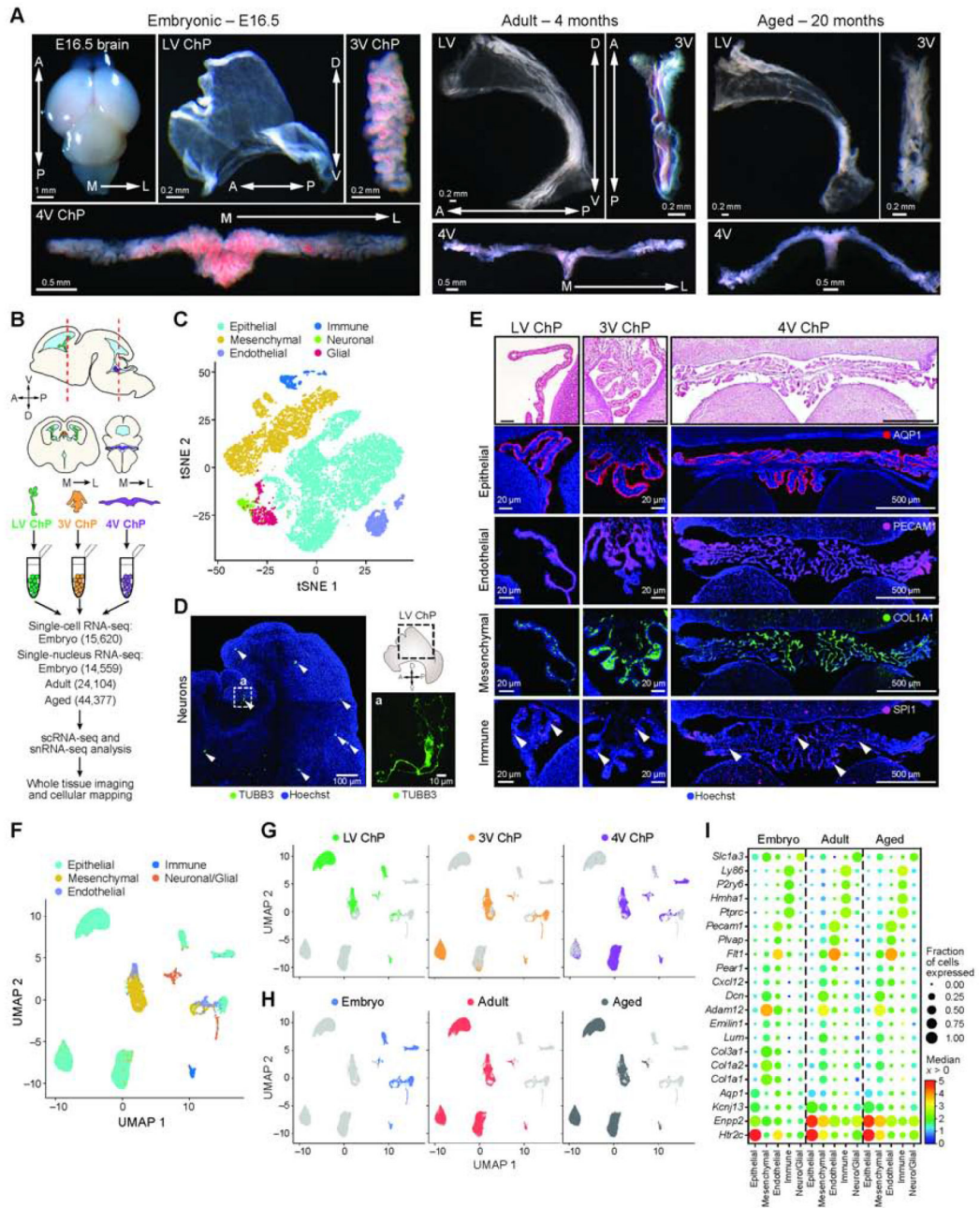
Figure 1. Single cell and single nucleus RNA-Seq of embryonic, adult, and aged ChPs.
(A) E16.5 brain and ChP from each ventricle in E16.5, adult, and aged brain. Arrows: anterior-posterior (A/P), dorso-ventral (D/V) and medial-lateral (M/L) axes. **(B)** Workflow. **(C)** Major cell types of E16.5 ChP. T-SNE of 15,620 single cell profiles (n = 9 mice, in pools of 3 animals per ventricle), colored by *post hoc* annotated cell type. **(D)** TUBB3-positive neurons (arrowheads) in E16.5 LV ChP. Inset *a*: High-magnification image. Schematic: dotted outline denotes region shown by immunostaining. Arrows: A/P and D/V axes. **(E)** Major cell type markers expressed in ChP. *Top:* H&E; *bottom*: Epithelial (AQP1), endothelial (PECAM1), mesenchymal (COL1A1) and immune cell (SPI1, arrowheads) immunostaining; Hoechst counterstain. **(F)** Major cell types of E16.5, adult, and aged ChP.

UMAP of 83,040 single nucleus profiles (snRNA-seq, n=17 mice. 2-4 animals per replicate of LV, 3V and 4V ChP from E16.5, adult and aged mice), colored by *post hoc* annotated cell type. **(G-H)** UMAP as in F, colored by ventricle (in G) or age (in H). **(I)** Cell type marker genes by snRNA-seq. Median expression level in expressing cells (color) and proportion of expressing cells (circle size) of selected genes (rows) in each major cell population (columns). See also Figure S1.
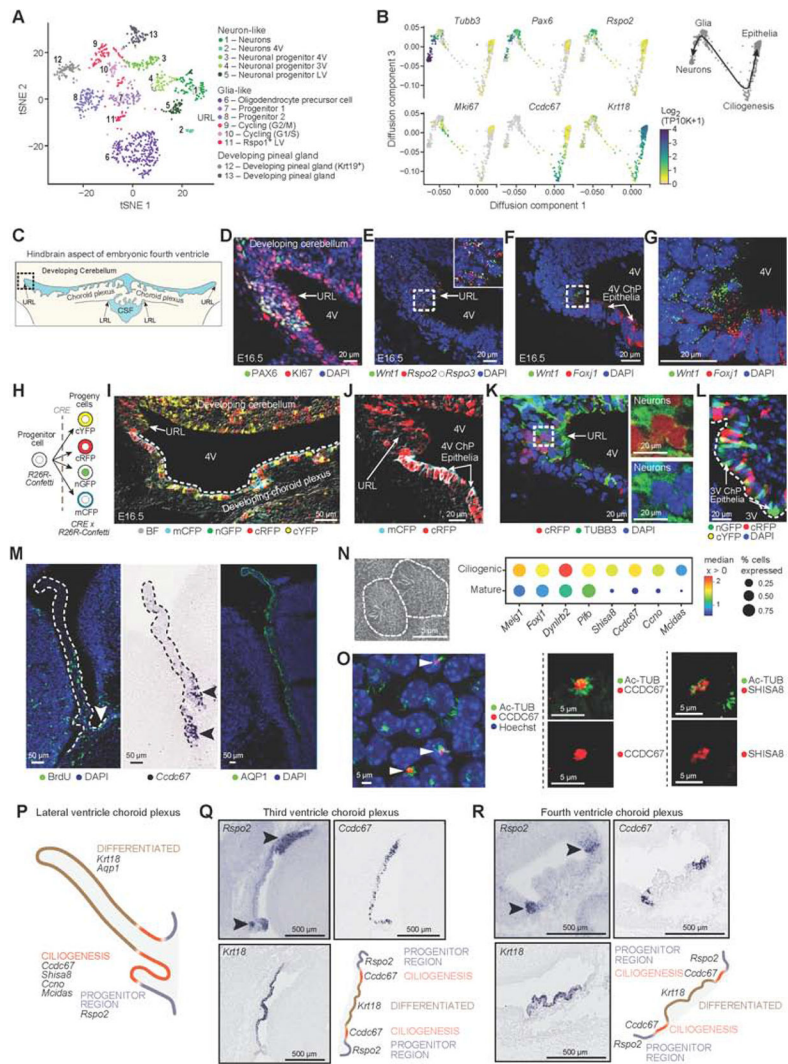
Figure 2. Epithelial differentiation trajectory reveals progenitor and ciliogenesis programs of ChP epithelial cells during development.

(**A**) Embryonic neuronal and glia-like cell subsets. T-SNE of embryonic neuronal and glia-like single cell profiles (scRNA-seq, 955 cells). (**B**) Diffusion map embedding (components 1 and 3) of neuronal, glia-like and epithelial cell profiles (dots) from 3V ChP, colored by $\log_2$(TP10K+1) expression of marker genes of neurons (*Tubb3*), progenitors (*Pax6, Rspo2*), cycling (*Mki67*), ciliogenesis (*Ccdc67*), and mature epithelial (*Krt18*) cells. *Right*: Suggested differentiation trajectories. (**C**) Schematic of embryonic hindbrain; upper rhombic lip (URL), lower rhombic lip (LRL). Dotted box: area shown in panels (**D-K**). (**D**) Proliferating (KI67) progenitors (PAX6) in URL. (**E**) SmFISH markers of progenitors (*Rspo2, Rspo3*) and *Wnt1*. (**F**) SmFISH of *Wnt1* and *FoxJ1*. (**G**) High magnification image of (F). (**H**) Confetti-labeling schematic. (**I**) E16.5 hindbrain region from *Wnt1-CRE2* crossed with Confetti mouse shows distribution of *Wnt1*-derived cells. (**J**) *Wnt1*-derived cRFP or mCFP epithelial cells adjacent to URL. (**K**) *Wnt1*-derived cRFP and TUBB3 neurons in URL with DAPI. Inset: split cRFP (*top*) and TUBB3 (*bottom*). (**L**) Confetti labeled cells in 3V ChP. (**M**) Proliferating cells enriched at LV ChP base. *Left*: BrdU

labeling; *Middle*: ISH of *Ccdc67*; *Right*: AQP1. **(N)** *Left*: Scanning EM of multi-ciliated epithelial cell. *Right:* Median expression level in expressing cells (color) and proportion of expressing cells (circle size) of markers of ciliogenesis (columns) in ciliogenic (developing) and mature epithelial cells (rows). **(O)** *Left*: LV ChP immunostained for Ac-Tubulin and CCDC67/DEUP1. *Middle and right*: Ac-Tubulin with CCDC67 (*middle*) or SHISA8 (*right*). **(P)** Schematic: LV ChP maturation regions. **(Q-R)** Spatial mapping of maturation domains in 3V and 4V ChP marked by progenitors (*Rspo2*), ciliogenesis (*Ccdc67*), differentiated epithelial cells (*Krt18*) (Genepaint). Schematic: ChP regions with maturing epithelial cells. See also Figure S2.
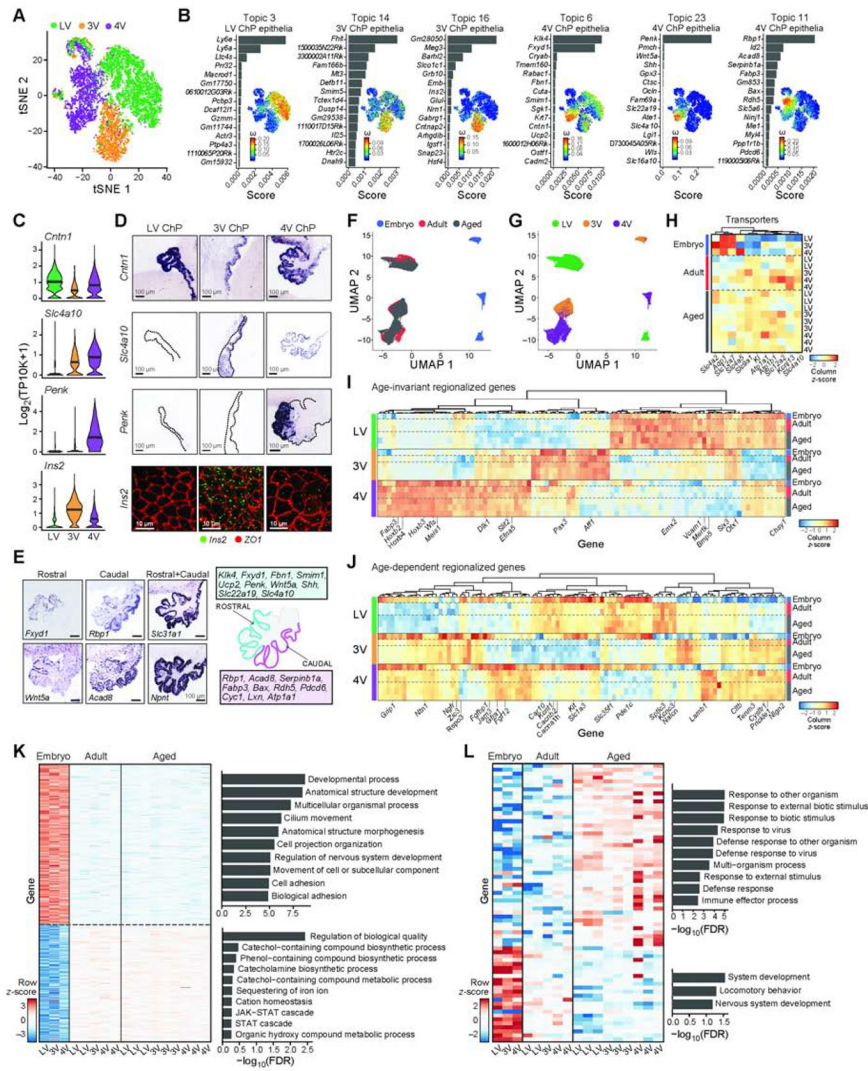
Figure 3. Regionalized epithelial transcriptional programs across ventricles and ages.
(A) Distinct embryonic epithelial cells clusters by ventricle. T-SNE of embryonic epithelial cell profiles (dots, scRNA-seq), colored by ventricle. **(B)** For each ventricle associated topic, shown is a bar plot of topic scores for top ranked genes (*left*), and t-SNE of the single cell profiles (as in A) colored by topic's weight per cell (*right*). **(C-D)** Regionalized genes in embryonic epithelial cells across ventricles. **(C)** Distribution of log$_2$(TP10K+1) expression of each gene across ventricles. **(D)** *Top rows*: Regionalized *mRNA* expression from Genepaint. *Bottom row*: *Ins2* smFISH. **(E)** Regionalized *mRNA* expression from Genepaint in 4V ChP with schematic. **(F-G)** T-SNE of single epithelial nucleus profiles colored by age (in **F**) or ventricle (in **G**). **(H)** Expression level scaled per gene (color scale) of transport and secretion genes, differential across ages (FDR<0.01) (see also (Xu et al., 2021) . **(I-J)** Heatmap of snRNA-seq data of differentially expressed genes across ventricles (FDR<0.01) that are age-invariant **(I)** or age-dependent **(J)**. Scaled expression level per gene (columns). *Left* color bar: ventricle. *Right* color bar: Age. **(K-L)** Age-dependent genes (snRNA-seq, FDR<0.01) between embryonic and mature (adult and aged, in **K**) or between adult and
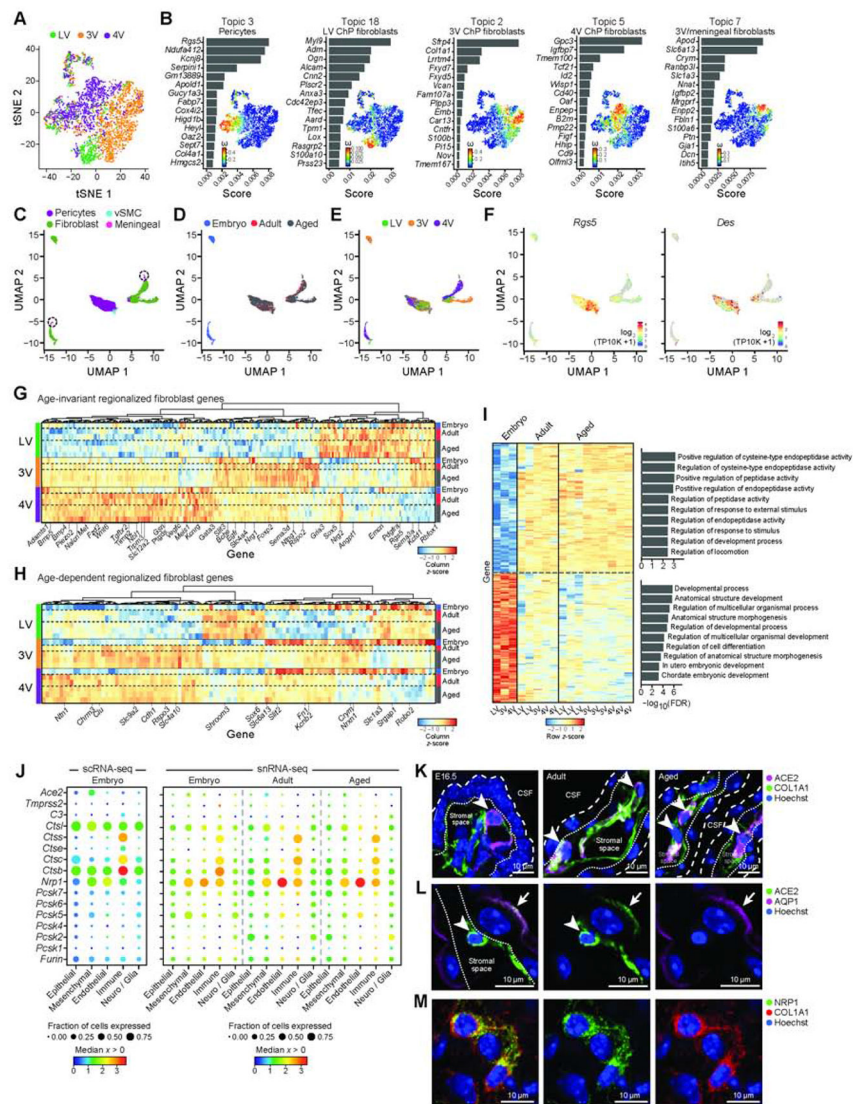
aged (in **L**). Average expression per sample across ventricles, scaled per gene (rows). *Right*: Enriched pathways per age-signature (hypergeometric p-value). See Figure S3.

Figure 4. Regionalized mesenchymal transcriptional programs across ventricles and ages.
(A) Embryonic mesenchymal cells largely cluster by ventricle. T-SNE of embryonic mesenchymal cell profiles (dots) colored by ventricle. **(B)** Ventricle associated topics with a mesenchymal subtype: a bar plot of topic scores for top ranked genes (*left*), and t-SNE (as in A) colored by topic's weight per cell (*right*) (topics associated with cycling cells in Figure S4B). **(C-E)** T-SNE of mesenchymal single nucleus profiles (dots), colored by cell type **(C)**, age **(D)**, and ventricle **(E)**, and $\log_2$(TP10K+1) expression of pericyte markers *Rgs5* and *Des* **(F)**. **(G-H)** Heatmap of snRNA-seq data of differentially expressed mesenchymal genes across ventricles (FDR<0.01) that are age-invariant **(G)** or age-dependent **(H)**. Scaled expression level per gene (columns). *Left* color bar: ventricle. *Right* color bar: Age. **(I)** Age-dependent genes (snRNA-seq, FDR<0.01) between embryonic and mature (adult and aged). Average expression per sample across ventricles, scaled per gene (rows). *Right*: Enriched pathways per age-signature (hypergeometric p-value). **(J)** SARS-CoV-2 cell entry and associated genes in embryonic scRNA-seq (*left*) and snRNA-seq (*right*). Median expression level in expressing cells (color) and proportion of expressing cells (circle size) of markers

(rows) across cell types (columns). **(K)** ACE2 expression in mesenchymal cells (COL1A1+) in 4V ChP. Coarse/fine dotted lines indicate apical/basal boundaries of epithelia. Arrowhead: ACE2+ cells. **(L)** ACE2 in adult epithelial cells (AQP1). Dotted line: base of epithelial cell. Arrowhead: stromal cell. Arrow: epithelial cell. **(M)** NRP1 expression in mesenchymal cells (COL1A1). See also Figure S4.
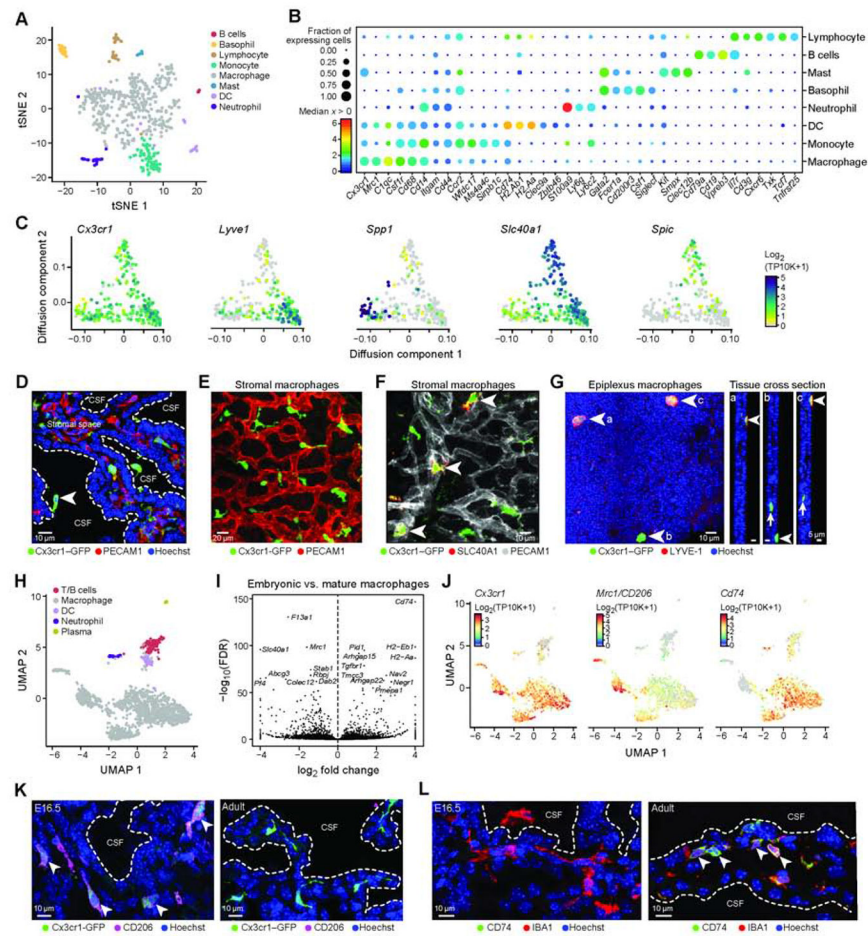
Figure 5. Immune cell diversity and macrophage niches within and across ChP

(**A**) Embryonic immune cell subsets in the ChP. T-SNE of embryonic immune single cell profiles, colored by cluster. (**B**) Median expression level in expressing cells (color) and proportion of expressing cells (circle size) of selected marker genes (columns) across immune cell subsets (rows). (**C**) Embryonic macrophage diversity. Diffusion map embedding of single cell macrophages, colored by $\log_2$(TP10K+1) expression of general macrophage marker (*Cx3cr1*) or of state specific genes (*Lyve1, Spp1, Slc40a1, Spic*). (**D**) *Cx3cr1^{+/GFP}* mouse LV ChP immunostained with PECAM1 (red) and Hoechst (blue). Arrowhead: epiplexus cells. Dotted line: ChP apical surface. (**E-F**) *Cx3cr1^{+/GFP}* LV ChP explant immunostained with PECAM1. (**F**) SLC40A1/FPN+ macrophages (arrowheads) along blood vessels. (**G**) *Left*: LYVE1+ epiplexus macrophages. *Right*: cross section at positions indicated by letters a, b and c in main panel. Arrows: stromal ChP macrophages. (**H**) UMAP of single immune nucleus profiles (dots), colored by immune cell type identity. (**I**) Volcano plot comparing embryonic to mature macrophages (snRNA-seq). (**J**) T-SNE of single immune nuclei (dots) colored by $\log_2$(TP10K+1) expression of genes marking macrophages (*Cx3cr1*), embryonically enriched gene (*Mrc1/CD206*) and adult enriched gene (*Cd74*). (**K**) *Cx3cr1^{+/GFP}* 4V ChP immunostained with MRC1 in embryo (E16.5, *left*) and adult (*right*). (**L**) 4V ChP immunostained with CD74 and IBA1 (E16.5, *left*) and adult
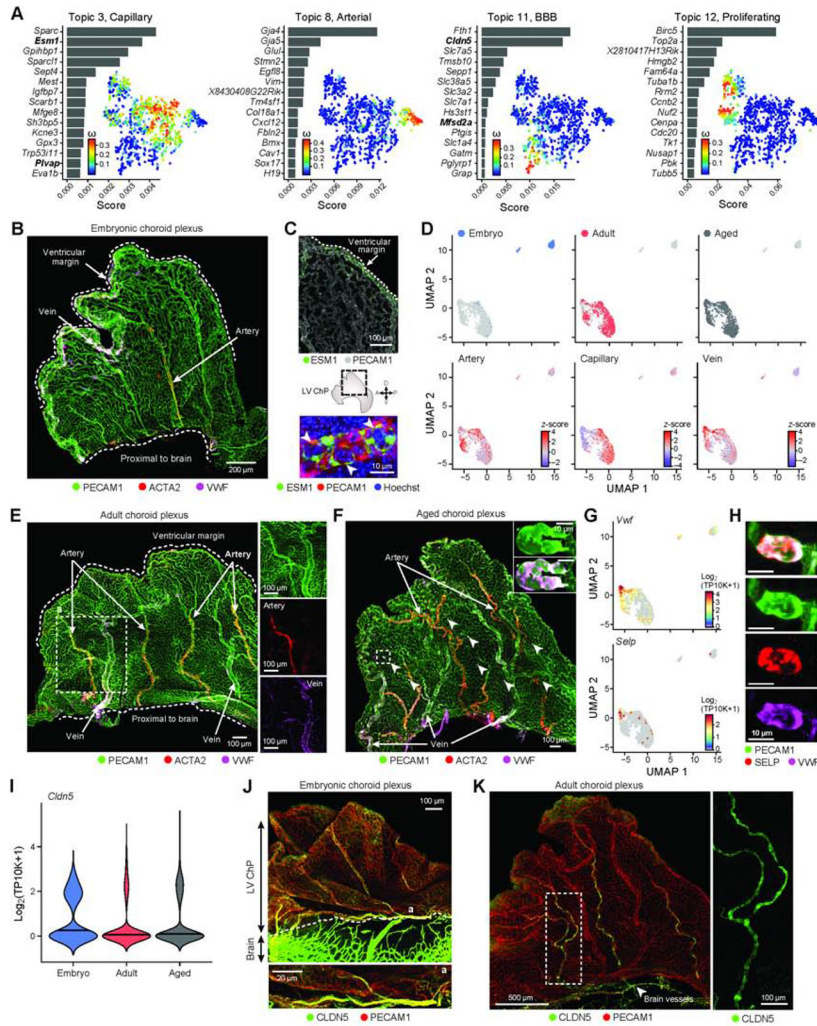
(*right*). **(K-L)** Arrowheads: stromal macrophages. Dotted line: epithelial apical boundary. See also Figure S5.

Figure 6. Vascular identity and BBB protein zonation within the ChP across ages.
(A) Embryonic endothelial cell transcriptional programs. For each topic, topic scores for top ranked genes (*left*) and t-SNE of single cell profiles colored by topic's weight per cell (*right*). **(B)** LV ChP immunostained with PECAM1, ACTA2 and VWF, marking the arterial (ACTA2+) and venous (ACTA2-, VWF+) vessels. **(C)** Angiogenic zonation. *Top:* LV ChP immunostained with PECAM1 and ESM1 (green). *Middle:* Dotted line: LV ChP free margin. Double headed arrows: A/P and D/V axes. *Bottom:* ESM1, PECAM1 and Hoechst. **(D)** UMAP of single endothelial nucleus profiles (dots) colored by age (top), endothelial subtype score (bottom). **(E)** LV ChP immunostained as in (B) reveal arterio-venous organization in adult. Dotted line: region of interest as inset. **(F)** Aged LV ChP immunostained as in (**B,E**). Arrowheads: VWF accumulation in vessels. Dotted line: region of interest as inset. Inset: elevated VWF expression. **(G)** UMAP (as in D), colored by log$_2$(TP10K+1) expression of genes *Vwf* and *Selp*. **(H)** Subset of aged vessels express VWF and SELP. **(I)** Distribution of *Cldn5* expression across ages. **(J)** Embryonic LV ChP immunostained with CLDN5 and PECAM1. Dotted line: brain-ChP border. *Bottom:* Vessel at position 'a'. **(K)** Adult LV ChP immunostained with CLDN5 and PECAM1. Arrowhead: CLDN5+ vessel at base of ChP. Dotted line: region enlarged on right. See also Figure S6.
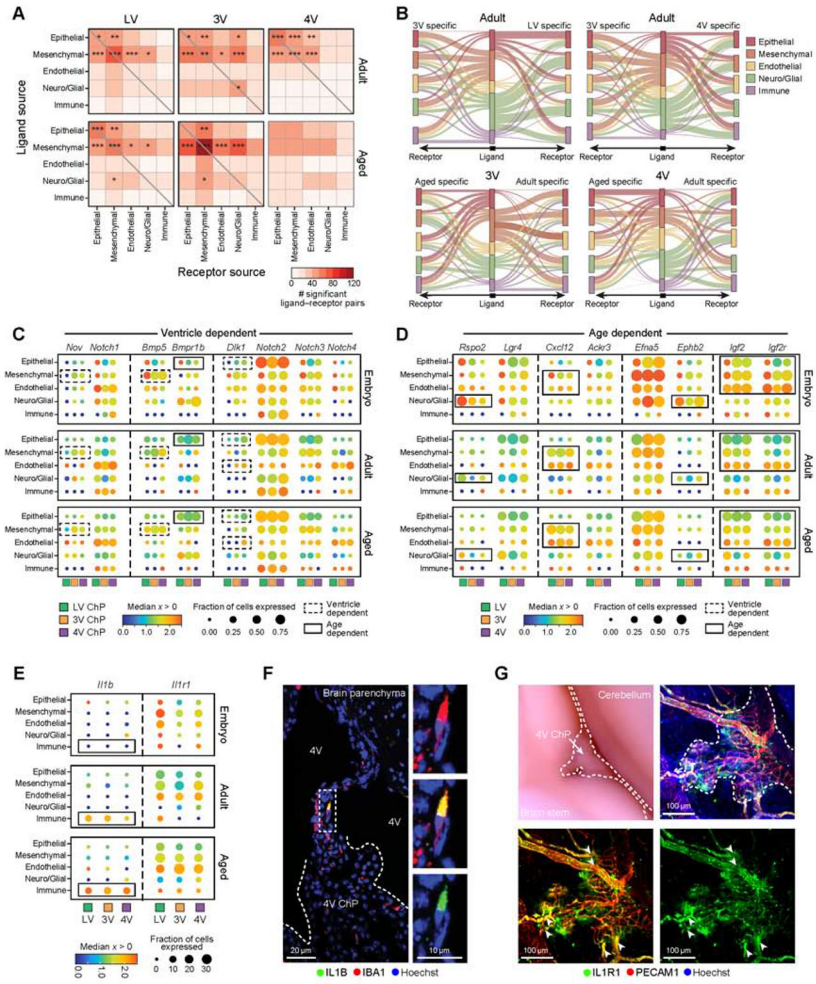
Figure 7. Mesenchymal, endothelial and immune cells contribute to cellular crosstalk in ChP.
(**A**) Number of statistically significant ligand-receptor pairs (LRPs, from CellPhoneDB (Efremova et al., 2020), STAR Methods) between pairs of ChP cell types, across ventricles in adult (*top*) and aged (*bottom*, embryo in Figure S7A). Significant pairs of cell types based on a randomization test marked as: *p 0.05, **p 0.01, ***p 0.001. (**B**) Differential LRPs across ventricles or ages. *Middle* bar: cell types expressing the ligand (color coded). *Right/left* bars: cell types expressing the corresponding receptor. Edge width: Number of LRPs in each cell type pair that are specific to the specific ventricle (*top*) or age (*bottom*). Edge color: cell-type (middle bar). (**C-E**) Selected ventricle-dependent and age-dependent LRPs. Median expression level in expressing cells (color) and proportion of expressing cells (circle size) in major cell population, across all ventricles (color coded) and ages (*top*: E16.5; *middle*: adult; *bottom*: aged). Dashed square: ventricle-dependent expression, solid line: age-dependent. Aging-dependent IL-1β-IL1R1 signaling (in **E**). (**F**) IL-1β immunostained macrophage in vessel like structures connecting ChP and brain parenchyma in aged brain. Inset: IL-1B macrophage. (**G**) *Left*: Whole mount aged hindbrain. Dotted lines outline 4V ChP. *Right*: IL1R1 immunostained endothelial cells (PECAM1) . Arrowheads: IL1R1+

blood vessels originating from the brain parenchyma and entering the ChP. See also Figure S7.

KEY RESOURCES TABLE

REAGENT or RESOURCE	SOURCE	IDENTIFIER
Antibodies		
Rat anti-BrdU	Abcam	#ab6326; RRID: AB_305426
Goat polyclonal anti-mouse ACE2	R&D Systems	#AF3437; RRID: AB_2223140
Mouse monoclonal anti-ACTA2-Cy3	Sigma-Aldrich	#C6198, RRID: AB_476856
Mouse monoclonal anti-AQP1	Santa Cruz	#32737; RRID: AB_626692
Rabbit polyclonal anti-CCDC67	Proteintech	#24579-1-AP
Goat polyclonal anti-CD62P/P-Selectin	R&D Systems	#AF737; RRID: AB_2285644
Rat monoclonal anti-CD74-488	Biolegend	#151005; RRID: AB_2750325
Mouse monoclonal anti-CLDN5-488	ThermoFisher	#352588; RRID: AB_2532189
Rabbit polyclonal anti-COL1A1	Abcam	#ab34710, RRID: AB_731684
Goat polyclonal Anti-ESM1	R&D Systems	#AF1999, RRID: AB_2101810
Chicken polyclonal anti-GFP	Abcam	#ab13970; RRID: AB_300798
Rabbit polyclonal anti-GFAP	Dako	#Z0334; RRID: AB_10013382
Rabbit polyclonal anti-IBA1	Wako	#019-19741, RRID: AB_839504
Hamster monoclonal anti-IL1B	Biolegend	#503513, RRID: AB_2814399
Goat polyclonal anti-IL1R1	R&D Systems	#AF771, RRID: AB_355587
Mouse monoclonal anti-KI67	BD PharMingen	#550609; RRID: AB_393778
Rat monoclonal anti-KI67	ThermoFisher	#14-5698-80; RRID: AB_10853185
Goat polyclonal anti-LYVE1	R&D Systems	#AF2125, RRID: AB_2297188
Rabbit polyclonal anti-MRC1/CD206	Abcam	#ab64693, RRID: AB_1523910
Goat polyclonal anti-NRP1	R&D Systems	#AF566; RRID: AB_355445
Rabbit polyclonal anti-PAX6	Millipore	#ab2237, RRID: AB_1587367
Rat monoclonal anti-PECAM1/CD31	BD PharMingen	#550274, RRID: AB_393571
Rabbit polyclonal anti-SHISA8	Abcam	#ab188621
Rat monoclonal anti-SPI1/PU.1	Novus Bio	#MAB7124-SP
Rabbit polyclonal anti-SPIC	ThermoFisher	#PA5-67537, RRID: AB_2692238
Rabbit anti-SLC40A1	Alpha Diagnostic International	#MTP11-A, RRID: AB_1619475
Mouse monoclonal anti-TUBB3	Biolegend	#801202, RRID: AB_10063408
Mouse monoclonal anti-Acetylated Tubulin	Sigma-Aldrich	T6793, RRID: AB_477585
Rabbit polyclonal anti-VWF	ThermoFisher	#MA5-14029; RRID: AB_305689
Rat monoclonal anti-WNT5A	R&D Systems	#MAB645; RRID: AB_10571221
Mouse monoclonal anti-ZO1	ThermoFisher	#33-9100; RRID: AB_2533147
Rabbit polyclonal anti-5HT	Sigma-Aldrich	#S5545; RRID: AB_477522
Chemicals, peptides, and recombinant proteins		
Collagenase II	GIBCO	17101-015
TrypLE	Life Technologies	12604
LIVE/DEAD staining kit	ThermoFisher	L-3224
10% Tween-20 (used for TST)	VWR Teknova	T0710
NP-40 Surfact-Amps Detergent Solution (used for NST)	ThermoFisher	28324
CHAPS, Molecular Biology Grade, (used for CST)	EMD Millipore	220201-1GM

REAGENT or RESOURCE	SOURCE	IDENTIFIER
Nuclei EZ Prep Nuclei Isolation Kit	Sigma	NUC101-1KT
Critical commercial assays		
10X Genomics Single Cell 3′ Gel Bead Kit V1	10X Genomics	PN-120231
10X Genomics Single Cell 3′ Gel Bead Kit V2	10X Genomics	PN-120237
10X Genomics Single Cell 3′ Gel Bead Kit V3	10X Genomics	PN-1000075
RNAscope Fluorescent Multiplex	ACD	#320851
Deposited data		
Raw and analyzed data	This paper	GEO: GSE168704
Experimental models: Organisms/strains		
Mouse: CD-1 (ICR)	Charles River Laboratories	Strain 022
Mouse: C57BL/6J	Jackson Laboratory	000664
Mouse: C57BL/6	Charles River Laboratories	N/A
Mouse: B6.129P2(Cg)-$Cx3cr1^{tm1Litt}$/J	Jackson Laboratory	005582
Mouse: 129S4.Cg-$E2f1^{Tg(Wnt1-cre)2Sor}$/J	Jackson Laboratory	002137
Mouse: $Gt(ROSA)\ 26Sor^{tm1(CAG-Brainbow2.1)Cle}$/J	Jackson Laboratory	013731
Oligonucleotides		
mm-$Axin2$-C3	ACD	400331-C3
mm-$FoxJ1$	ACD	317091
mm-$Ins2$-C2	ACD	310751-C2
mm-$Rspo1$	ACD	401991
mm-$Rspo2$-C2	ACD	402001-C2
mm-$Rspo3$-C3	ACD	402011-C3
mm-$Wnt1$	ACD	401091
mm-$Wnt2b$-C2	ACD	405031-C2
mm-$Wnt3a$	ACD	405041
mm-$Wnt5a$-C3	ACD	316791-C3
Software and algorithms		
Cellranger	https://support.10xgenomics.com/single-cell-gene-expression/software/overview/welcome	N/A
CellPhoneDB	Efremova et al., 2020	N/A
Seurat	https://github.com/satijalab/seurat	N/A
R	https://www.r-project.org/	N/A
Other		
Noyes Spring Scissors – Tungsten Carbide/Straight	Fine Science Tools	#15514-12
Dounce Tissue Grinder Set	Sigma	#D8938-1SET